Journal of Geophysical Research: Solid Earth

RESEARCH ARTICLE
10.1029/2018JB016032

Stochastic Inversion of *P*-to-*S* Converted Waves for Mantle Composition and Thermal Structure: Methodology and Application

F. D. Munch[1], **A. Khan**[1], **B. Tauzin**[2,3], **A. Zunino**[4], **and D. Giardini**[1]

[1]Institute of Geophysics, ETH Zurich, Zurich, Switzerland, [2]Université de Lyon, UCBL, ENS Lyon, CNRS, Laboratoire de Géologie de Lyon, Terre, Planètes, Environnement, Villeurbanne, France, [3]Research School of Earth Sciences, Australian National University, Canberra, Australia, [4]Niels Bohr Institute, University of Copenhagen, Copenhagen, Denmark

Abstract We present a new methodology for inverting *P*-to-*S* receiver function (RF) waveforms directly for mantle temperature and composition. This is achieved by interfacing the geophysical inversion with self-consistent mineral phase equilibria calculations from which rock mineralogy and its elastic properties are predicted as a function of pressure, temperature, and bulk composition. This approach anchors temperatures, composition, seismic properties, and discontinuities that are in mineral physics data, while permitting the simultaneous use of geophysical inverse methods to optimize models of seismic properties to match RF waveforms. Resultant estimates of transition zone (TZ) topography and volumetric seismic velocities are independent of tomographic models usually required for correcting for upper mantle structure. We considered two end-member compositional models: the equilibrated equilibrium assemblage (EA) and the disequilibrated mechanical mixture (MM) models. Thermal variations were found to influence arrival times of computed RF waveforms, whereas compositional variations affected amplitudes of waves converted at the TZ discontinuities. The robustness of the inversion strategy was tested by performing a set of synthetic inversions in which crustal structure was assumed both fixed and variable. These tests indicate that unaccounted-for crustal structure strongly affects the retrieval of mantle properties, calling for a two-step strategy presented herein to simultaneously recover both crustal and mantle parameters. As a proof of concept, the methodology is applied to data from two stations located in the Siberian and East European continental platforms.

Key Points:
- We present a new tool for inversion of *P*-to-*S* receiver function waveforms to probe mantle temperature and composition
- The method allows for self-consistent determination of depth, sharpness, and velocity contrast at seismic discontinuities
- We account for the effects of seismic processing, crustal structure, and seismic attenuation on receiver function waveforms

Supporting Information:
- Supporting Information S1

Correspondence to:
F. D. Munch,
federico.munch@erdw.ethz.ch

Citation:
Munch, F. D., Khan, A., Tauzin, B., Zunino, A., & Giardini, D. (2018). Stochastic inversion of *P*-to-*S* converted waves for mantle composition and thermal structure: Methodology and application. *Journal of Geophysical Research: Solid Earth*, *123*, 10,706–10,726. https://doi.org/10.1029/2018JB016032

Received 30 APR 2018
Accepted 5 OCT 2018
Accepted article online 10 OCT 2018
Published online 10 DEC 2018

1. Introduction

P-to-*S* converted waves are teleseismic *P* waves that convert a portion of their energy into *S* waves when encountering a discontinuity in material properties. Such converted waves are recorded as part of the *P* wave coda and contain a significant amount of information on the seismic structure beneath the receiver. However, they are strongly influenced by the seismic source signature and the structure encountered along their propagation path through the mantle. These influences can be eliminated by deconvolving the vertical component v(t) from the radial component r(t) (Phinney, 1964). The result is a time series called the receiver function (RF) (Langston, 1979) where time is a proxy for depth and positive (or negative) amplitudes roughly correspond to an increase (or decrease) in shear-wave velocities.

RF waveforms are mostly sensitivity to the shape of velocity gradients and contain little information on absolute velocities (Rondenay, 2009). Constraints on absolute velocities are typically gained by adding a priori information from a global/regional seismic model (e.g., Ammon et ., 1990) or by combining RF waveforms with other geophysical observables such as surface wave group and phase velocities (e.g., Calò et al., 2016; Moorkamp et al., 2010; Shen et al., 2013). More commonly, RF waveforms are used to identify discontinuities in seismic velocities such as the Moho (e.g., Calò et al., 2016; Kind & Vinnik, 1988; Langston & Hammer, 2001; Lodge & Helffrich, 2009; Lombardi et al., 2009), the lithosphere-asthenosphere boundary (Heit et al., 2007; Kind et al., 2012; Kumar et al., 2012; Sodoudi et al., 2006), and the 410- and 660-km discontinuities (Cottaar & Deuss, 2016; Lawrence & Shearer, 2006a; Tauzin et al., 2008; Vinnik et al., 2009). The latter discontinuities are the most seismically visible features of the mantle transition zone (TZ). The 410-km discontinuity reflects the exothermic olivine→wadsleyite phase transition, and the 660-km discontinuity is mainly produced by the

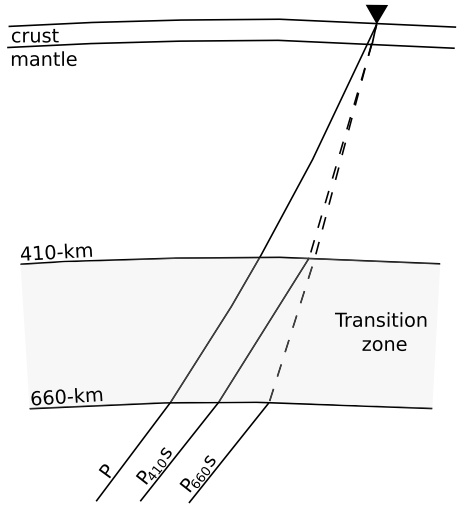

Figure 1. Schematic representation of teleseismic *P*-to-*S* waves scattered in the mantle transition zone and recorded at a seismic station (black triangle). Solid and dashed lines correspond to *P* and *S* ray path segments, respectively. Figure modified from Schmandt (2012).

endothermic ringwoodite→bridgmanite + ferropericlase transition (Ringwood, 1975). As these phase transitions are sensitive to variations in mantle thermo-chemical state, changes in temperature or composition affect location and sharpness of the discontinuities and TZ velocity gradients (e.g., Bina & Helffrich, 1994; Khan et al., 2009; Shearer, 2000).

As shown in Figure 1, P410s and P660s correspond *P*-to-*S* waves converted at the 410- and 660-km discontinuities, respectively. These converted waves can be used to map variations in the sharpness and depth range of velocity gradients in the mantle TZ (e.g., Helffrich, 2000; Lawrence & Shearer, 2006b; Schmandt, 2012). In this context, previous studies have mapped both regional (e.g., Cao & Levander, 2010; Chen & Ai, 2009; Farra & Vinnik, 2000; Owens et al., 2000) and global (e.g., Chevrot et al., 1999; Lawrence & Shearer, 2006a; Tauzin et al., 2008) variations in TZ thickness and velocity. Interpretation of the inferred variations in terms of mantle temperatures are typically reported as deviations from an arbitrarily chosen reference geotherm (e.g., Cottaar & Deuss, 2016; Deuss et al., 2006; Deuss et al., 2013; Tauzin & Ricard, 2014) and are often based on knowledge of the Clapeyron slope for pure $(Mg,Fe)_2SiO_4$-phases but neglect the contribution from other phases (e.g., pyroxene and garnet; Owens et al., 2000; Tauzin et al., 2013).

Here we describe a strategy to determine composition, thermal state, mineralogy, and seismic properties of Earth's mantle, directly from the inversion of *P*-to-*S* converted waves in the form of RF waveforms. The inversion scheme makes use of self-consistent mineral phase equilibria calculations from which rock mineralogy, and ultimately its elastic properties, can be predicted as a function of pressure, temperature, and bulk composition from thermodynamic data. The advantage of this approach is that it inserts plausible geophysical/petrological knowledge of seismic discontinuities, while permitting the simultaneous use of geophysical inverse methods to optimize profiles of physical properties (e.g., bulk and shear modulus and density) to match geophysical data (e.g., Afonso et al., 2013; Cammarano et al., 2005; Cobden et al., 2008; Drilleau et al., 2013; Khan et al., 2006; Khan et al., 2009; Stixrude & Lithgow-Bertelloni, 2005a; Tirone et al., 2009). As an illustration hereof, Khan et al. (2013) used surface-wave phase-velocity dispersion data to directly image upper mantle Mg/Fe and Mg/Si variations and topography on the 410-km discontinuity beneath the Australian continent. This study showed that (1) compositional effects could not be excluded even at long wavelengths and (2) the thermochemically induced phase transformations strongly contribute to lateral variations in structure and topography across the 410-km discontinuity (see also Zunino et al., 2016). In contrast to estimation of TZ topography and thickness derived from RF migration (e.g., Cottaar & Deuss, 2016; Tauzin et al., 2013), the methodology proposed here does not require the use of a tomographic model to correct for crustal and upper mantle effects. While a previous study (e.g., Ritsema, Cupillard, et al., 2009) only attempted to map effects related to temperature variations in the upper mantle from comparison of theoretical and observed differential travel times between P410s and P and between P660s and P410s, we perform a systematic study that considers variations in the entire RF waveform with respect to all relevant parameters.

In summary, in the present study we wish to extend the methodology employed by Khan et al. (2013) to invert RF waveforms directly for mantle thermo-chemical parameters with the ultimate goal of improving constraints on TZ structure. Synthetic RF waveforms are computed from the thermodynamically predicted velocity profiles as described in sections 3 and 4. The inverse problem is solved by combining a Markov chain Monte Carlo (McMC) method with a stochastic optimization technique (section 5). We first performed a series of synthetic tests (sections 6) in order to examine the effectiveness and robustness of the proposed approach. Finally, as a proof of concept, we apply the proposed strategy to retrieve crustal and mantle structure beneath two permanent stations located in two distinct stable continental regions.

2. Model Parameterization

2.1. Computation of Mantle Mineral Phase Equilibria

Mineralogical models of the Earth typically view the mantle as either homogeneous and pyrolitic (Bass, 1995; Francis, 1987; Ringwood, 1975) or chemically stratified with homogeneous and equilibrated

Table 1
CFMASNa Basalt $\mathbf{X_B}$ *and Harzburgite* $\mathbf{X_H}$ *End-Member Model Compositions (in wt%)*[a]

Component	$\mathbf{X_B}$	$\mathbf{X_H}$
CaO	13.05	0.50
FeO	7.68	7.83
MgO	10.49	46.36
Al_2O_3	16.08	0.65
SiO_2	50.39	43.64
Na_2O	1.87	0.01

[a]Taken From Khan et al. (2009).

compositions in each layer (e.g., Mattern et al., 2005). To first order, such models are capable of explaining the observed composition of mid-ocean ridge basalts (Chen et al., 1991; Frey et al., 1978; McKenzie & Bickle, 1988) and seismic velocities of the upper mantle and TZ (Irifune, 1993; Ita & Stixrude, 1992; Weidner, 1985). However, experimental measurements of mantle mineral chemical diffusivity (e.g., Hofmann & Hart, 1978) suggest that equilibration may not be accomplished over the age of the Earth for the amount of stretching and folding predicted in mantle convection simulations (e.g., Brandenburg & van Keken, 2007; Davies, 2006; Nakagawa & Buffett, 2005; Xie & Tackley, 2004). Moreover, trace element chemistry of basalts (e.g., Hofmann & White, 1982; Sobolev et al., 2007) and analysis of scattered seismic waves (e.g., Bentham & Rost, 2014; Hedlin et al., 1997; Helffrich, 2006; Tauzin et al., 2017) also point to the mantle as consisting of a mechanical mixture.

Xu et al. (2008) explored the effect of major element disequilibrium on seismological properties of the mantle. The authors considered two types of mantle compositional models: mechanical mixture and equilibrium assemblage. The former represents the scenario in which pyrolitic mantle has undergone complete differentiation to basaltic and harzburgitic rocks. The bulk properties of this model are computed as the Voigt-Reuss-Hill average (Watt et al., 1976) of the properties of the minerals in the basaltic and harzburgitic end-members. In contrast, bulk properties of the equilibrium model are computed based on the mineralogy of the averaged bulk composition. Xu et al. (2008) demonstrated that even with identical bulk compositions, an equilibrium assemblage and a mechanical mixture result in different mineral modes and, as a consequence, different bulk S, *P* wave velocities (V_s and V_p, respectively), and densities (ρ). The authors also reported that mechanically mixed models are characterized by faster *S* wave velocities as well as sharper velocity gradients.

In view of this and to test these models quantitatively against data, here we consider both the equilibrium assemblage (EA) and mechanical mixture (MM) model. The mineralogy for the EA model is defined as

$$\phi[\mathrm{f}\,\mathbf{X_B} + (1-\mathrm{f})\,\mathbf{X_H}], \tag{1}$$

and the phase assemblage for the MM model is given by

$$\mathrm{f}\,\phi[\mathbf{X_B}] + (1-\mathrm{f})\,\phi[\mathbf{X_H}], \tag{2}$$

where ϕ corresponds to the phase proportions given the bulk compositions of basalt $\mathbf{X_B}$, harzburgite $\mathbf{X_H}$, and the basalt fraction f. For the purpose of this work, we follow Xu et al. (2008) and consider the mantle to be compositionally homogeneous. The choice of basalt and harzburgite as end-members of mantle composition relies on crust formation processes at mid-ocean ridges. To first order, mid-ocean ridges represent the major source of chemical differentiation of the Earth's mantle. At ridges, partial melting generates a basaltic crust leaving behind its depleted complement, harzburgite (McKenzie & Bickle, 1988). The resulting physically and chemically stratified oceanic lithosphere is then cycled back into the mantle at subduction zones, becomes entrained in the mantle flow and remixes (e.g., Tackley et al., 2005). In this work, basalt and harzburgite compositions are described using the CFMASNa model chemical system comprising the oxides CaO-MgO-FeO-Al_2O_3-SiO_2-Na_2O (Table 1); which account for ~98% of the mass of Earth's mantle (e.g., Irifune, 1994).

Mantle thermal structure is described by an adiabatic geotherm underneath a conductive lithosphere. The lithospheric temperature is estimated as a linear gradient defined by the temperature (T_0) at the surface and the temperature (T_{lit}) at the bottom of the lithosphere (z_{lit}); where z_{lit} is defined as the depth at which the conductive lithospheric geotherm intersects the mantle adiabat defined by the entropy of the lithology at the temperature T_{lit} and pressure P_{lit}. The pressure profile is obtained by integrating the load from the surface.

We combine the free-energy minimization strategy described by Connolly (2009) with the self-consistent thermodynamic formulation of Stixrude and Lithgow-Bertelloni (2005b) and the parameters given by Stixrude and Lithgow-Bertelloni (2011) to estimate rock mineralogy, seismic velocities, and density as a function of pressure, temperature, and bulk composition. The free-energy minimization can be carried out in two ways: by dynamic or by static implementation. Dynamic implementation means minimizing the Gibbs free-energy of the system at a particular value of pressure, temperature, and composition during the

inversion process (e.g., Afonso et al., 2013; Chust et al., 2017; Duesterhoeft & Capitani, 2013; Duesterhoeft et al., 2014; Khan et al., 2006). Alternatively in the static implementation, physical properties are calculated for a certain range of pressure-temperature conditions and stored in tables prior to the solution of the inverse problem (e.g., Zunino et al., 2011). Zunino et al. (2011) developed the Python/Fortran package PHEMGP (https://github.com/inverseproblem/Phemgp) that allows fast recovery of bulk rock properties by assembling three-dimensional (pressure-temperature-composition) tables from two-dimensional (pressure-temperature) precomputed tables for single compositions.

Static implementation is very suitable for computing properties in a mechanically mixed mantle because only tables for basalt and harzburgite are needed to calculate properties as a continuous function of mantle composition. A resolution of 0.1 in f is necessary to reproduce velocities in the equilibrium model with the accuracy required for most geophysical applications (Zunino et al., 2011). In the present study, we employ a static implementation (PHEMGP) for computing properties in MM models and a dynamic implementation based on the software Perple_X (http://perplex.ethz.ch/) for calculation of mantle properties in EA models.

The present thermodynamic model of Stixrude & Lithgow-Bertelloni, (2005b, 2011) has limitations. First, the equilibrium assumption is dubious at low temperatures because equilibrium might not be achieved (e.g., Wood & Holloway, 1984). Consequently, mineralogy for temperature below 800 °C is computed at 800 °C. The resultant mineralogy is then used to calculate physical properties at the temperature of interest. Second, deviations from adiabatic temperature profiles due to radioactive heating and thermal boundary layers induced by phase transitions are neglected (Stixrude & Lithgow-Bertelloni, 2011). The thermodynamic model presented here precludes consideration of redox effects (e.g., Cline et al., 2018) as well as minor phases and components such as H_2O and melt due to lack of thermodynamic data. Density and elastic moduli are estimated to be accurate to within ~0.5% and ~1–2%, respectively (Connolly & Khan, 2016).

Although it is difficult to quantify the error produced by neglecting H_2O, experimental evidence suggests that the presence of H_2O would tend to thicken the TZ by moving the olivine-wadsleyite transition up (e.g., Frost & Dolejš, 2007) while deepening the dissociation of ringwoodite (Ghosh et al., 2013). Furthermore, the presence of H_2O is expected to reduce seismic velocities due to the weakened chemical bonding by hydrogen (Karato, 2010). However, experimental studies suggest that the influence of water on high-frequency elastic wave velocities is minor (<0.1%) for water content less than ~0.1wt% at relevant mantle conditions (e.g., Chang et al., 2015; Mao et al., 2008; Schulze et al., 2018; Thio et al., 2015). In addition to changes in phase equilibria, the solidus decreases with increasing water content (e.g., Hirschmann, 2010; Litasov, 2011). Therefore, a hydrated TZ could also result in dehydration-induced partial melting on top of the 410-km and underneath the 660-km discontinuity (e.g., Bercovici & Karato, 2003; Schmandt et al., 2014). These effects could potentially be significant in regions around subduction zones.

2.2. Crustal Structure

In the present study, crustal structure is not modeled in terms of the thermo-chemical parameterization because the thermodynamic database considered here comprises only mantle minerals (Stixrude & Lithgow-Bertelloni, 2011). Instead, crustal structure beneath each station is parameterized in terms of five layers with variable *S* wave velocity V_s^i and thickness d_i. Crustal velocities are assumed to increase as a function of depth ($V_s^1 < V_s^2 < V_s^3 < V_s^4 < V_s^5 < V_s^{Moho}$) with *S* wave velocity below the Moho V_s^{Moho} determined by the mantle compositional and thermal structure (see section 2.1). As discussed by Roy and Romanowicz (2017), the choice of crustal V_p/V_s ratio does not significantly affect the recovery of crustal velocity models. Therefore, crustal *P* wave velocities and densities are computed using V_p/V_s and ρ/V_s ratios taken from PREM (Dziewonski & Anderson, 1981).

3. Data Processing

The data consist of three-component seismograms recorded at two broad-band permanent stations (see Figure 2a) between 1976 and 2016. To ensure a good signal-to-noise ratio, we selected teleseismic events occurring at epicentral distances (Δ) between 40° and 95° with magnitudes larger than 5.5.

The records are first band-pass filtered using a Butterworth filter in the period range 1–100 s. Afterwards, the incident and scattered wavefields are separated by rotation of the three orthogonal components of the seismogram (N-S, E-W, and vertical) into radial (R), transverse (T), and vertical (Z) components. After rotation, the ratio between the maximum amplitude of the signal (measured on the vertical component in the time window

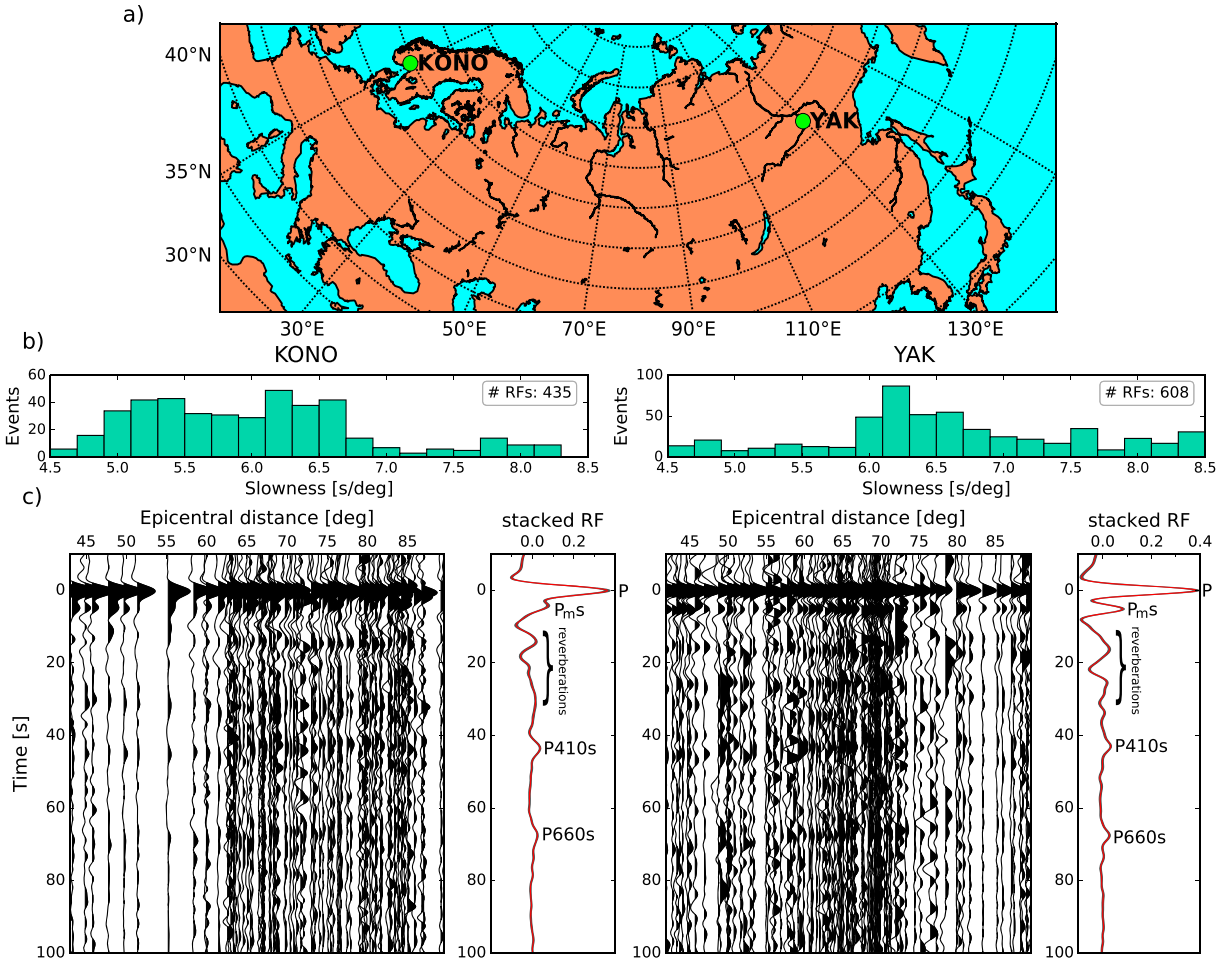

Figure 2. (a) Map showing geographical location of the two seismic stations considered in this study: Yakutsk (YAK) and Kongsberg (KONO). (b) Distribution of slownesses of the *P* wave recorded at KONO (left) and YAK (right). (c) Receiver function (RF) waveforms observed at KONO (left) and YAK (right) as a function of epicentral distance before move-out correction, resulting mean stacks (red), and uncertainties $\delta \mathrm{RF}^{\mathrm{obs}}(t)$ estimated using bootstrap resampling (black, almost indistinct from the mean).

$t_p - 5\mathrm{s} < t < t_p + 25\mathrm{s}$, where t_p is the theoretical *P* wave arrival) and the averaged root-mean-square of the vertical component is computed. All seismograms for which this ratio is lower than 5 are discarded. The selected traces are then trimmed to the time window ($t_\mathrm{p} - 50$ s, $t_\mathrm{p} + 150$ s) and iterative time-domain deconvolution (Ligorria & Ammon, 1999) is applied to deconvolve the Z and R components. Time-domain deconvolution is performed by progressively constructing the Earth's impulse response through iterative cross-correlation between the observed radial component and source wavelet (vertical component), and extraction of the highest correlated signal at each iteration. This approach has the advantage of providing long-period stability and requiring causality in the recovered RF waveforms (Ligorria & Ammon, 1999; Rondenay, 2009).

As the amplitudes of P410s and P660s are considerably smaller compared to the *P* wave amplitude, the signal-to-noise ratio must be increased to guarantee the detectability of the converted waves (Rondenay, 2009). This can be achieved by stacking a large number of RF waveforms. Prior to stacking, RF waveforms are low-pass filtered to remove frequencies higher than 0.2 Hz. Frequencies higher than 0.2 Hz are removed because the amplitude of TZ conversions on stacked waveforms significantly decreases at higher frequencies due to environmental noise, signal processing effects, and the effect of 3-D heterogeneities on travel-times. The stacking procedure averages hundreds of RF waveforms from different events recorded at a station and thus characterized by different epicentral distances, ray parameters (slownesses) of the *P* wave, and therefore *P* wave incidence angles. As the path of *P* and *S* waves between the interface of conversion and the surface have different lengths depending on the angle of incidence, a curvature (move-out) is observed in the differential travel time between the conversion and the *P* wave. In order to coherently stack the converted waves,

a correction for this curvature (move-out correction) should be applied prior to stacking. The move-out correction is here computed for the IASP91 (Kennett & Engdahl, 1991) velocity model at a reference slowness of 6.5 s/deg, which corresponds to a reference epicentral distance of ~ 65°. Finally, errors on stacked amplitudes $\delta RF^{obs}(t)$ (2 standard deviations) are estimated using a bootstrap resampling approach (Efron & Tibshirani, 1991). In order to test the influence of the velocity model used for the move-out correction on the final stacks, we computed corrections for IASP91 and a best-fitting velocity model (to be described in the following). Differences in the resulting waveforms (see Figure S1 in supporting information) were found to be negligible in comparison to $\delta RF^{obs}(t)$.

Figure 2c depicts observed RF waveforms as a function of epicentral distance before move-out correction, and the corresponding final move-out corrected stack for the two stations located in Figure 2a. Both conversions of interest at the 410- and 660-km discontinuities, P410s and P660s, appear on individual RF waveforms at roughly 40 and 70 s after the *P* wave. The strong conversion at the Moho discontinuity (Pms) and the multiple reverberations within the crust are at the origin of the strong amplitudes in the early part of the RF waveform.

4. Computation of Synthetic RFs

4.1. Method

In the following, synthetic waveforms (frequency range: 0.01 – 0.3 Hz) for 25 slownesses (see section 4.2) are computed using the reflectivity method (Fuchs & Müller, 1971; Muller, 1985) and subsequently filtered, deconvolved, and stacked using identical methods to those applied to the observed seismograms (section 3). Applying identical methods to both observed and synthetic seismograms is essential for modeling RF waveforms as accurately as possible. The reflectivity method is based on numerical integration of the plane wave reflection coefficient (reflectivity) of a layered medium in the frequency-slowness domain and subsequent multiplication with the source spectrum to obtain synthetic seismograms. The method allows for modeling the full propagation from source to receiver and not only includes transmitted and converted waves but also accounts for the interference of different phases (e.g., PP and PcP), surface multiples, and deviations of the wavefront from a plane wave at a moderate computational cost (~45 s per velocity model). As the source influence is removed by the deconvolution, the source characteristics do not have a significant effect on the synthetic RF waveforms. Hence, we model the source as a punctual explosion located at 25 km depth with time signature given by a Heaviside step function. The choice of source depth does not introduce artifacts in the stacked RF waveforms because the depth phases (pP and pS) have a completely different move-out curvature relative to direct conversions across the deconvolved time-slowness section and thus stack incoherently. The resulting RF waveforms have been benchmarked against RF waveforms computed using synthetic seismograms obtained by full waveform modeling methods (Krischer et al., 2017; Van Driel et al., 2015), see Figure S2.

4.2. Slowness Distribution

As the transmission coefficients and, consequently, amplitudes of *P*-to-*S* conversions depend on the angle of incidence (Aki & Richards, 2002), replication of the observed slowness distribution (SD) is essential for proper modeling of converted amplitudes. However, each stacked RF is typically composed of hundreds of single observations characterized by different incidence angles making the computation of synthetic RF waveforms for the entire range of observed slownesses computationally demanding. Here we propose an alternative strategy to properly model converted amplitudes with relatively low computational cost. The proposed scheme consists of (1) discretization of the SD into 25 evenly spaced slowness intervals, (2) estimation of the mean observed slowness p_i as well as the number of slownesses N_i in each interval, (3) computation of synthetic RF waveforms for all estimated p_i, and (4) move-out correction and stacking of synthetic RF waveforms weighting each RF according to N_i.

Figure 3 illustrates the importance of correctly accounting for the observed slowness distribution. Figure 3a shows the observed SD for KONO seismic station (orange), the discretized SD (black) obtained by the scheme presented above, and a uniform SD (blue). Additionally, Figure 3b depicts the stacked RF waveforms computed for the corresponding SD using the IASP91 velocity model (Kennett & Engdahl, 1991). No considerable time differences are observed between the computed stacks. However, the estimated P410s (~ 44 s) and P660s (~ 68 s) amplitudes significantly depend on the SD considered. In particular, computed amplitudes are underestimated when a uniform SD is assumed. That P660s is more affected than P410s can be attributed to the fact that the range of incidence angle is larger for the 660-km discontinuity making variations in conversion amplitude larger.

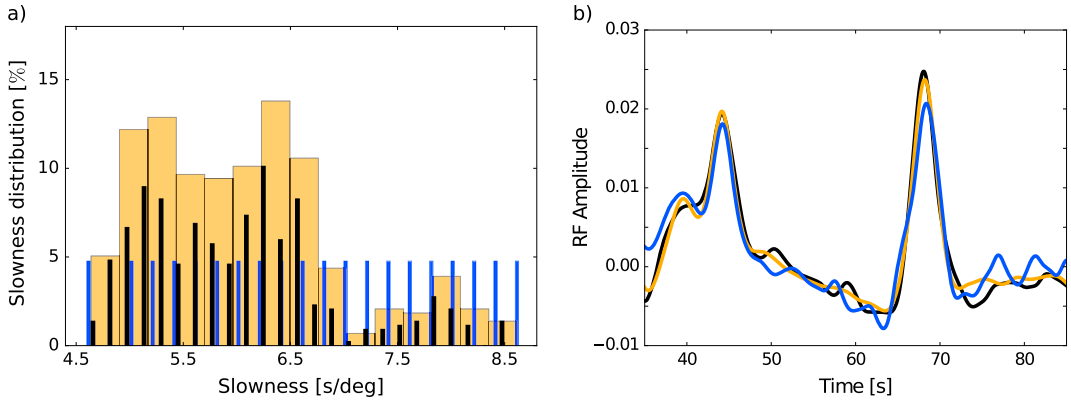

Figure 3. Influence of slowness distribution (SD) on the stacked receiver function (RF). (a) SD recorded at KONO seismic station (orange), uniform SD (blue), and an approximation of KONO SD using 25 representative slowness values (black). (b) stacked RF waveforms obtained for each of the aforementioned SD using the IASP91 velocity model (Kennett & Engdahl, 1991).

This example illustrates how inaccurate modeling of the observed slowness distribution can result in significant deviations of the mean slowness and, consequently, amplitudes of conversion. Therefore, the observational slowness distribution must be accurately replicated when inverting RF amplitudes. In this regard, the choice of reference slowness and velocity model used for computing the move-out correction is not significant while identical reference slownesses and velocity models are used on the observed and modeled RF waveforms. Alternatively, the dependency of stacked amplitudes on the heterogeneity of the observed slowness SD could be addressed during data processing. For instance, by partially stacking the observed RF waveforms into bins of slowness and subsequent stacking of the partial stacks. The resulting stack would be less dependent on the heterogeneity of the observed SD. However, such a strategy would potentially increase the weight of noisy data on the final stack. Alternative data processing schemes should be explored, but this is beyond the scope of this work.

4.3. Attenuation

As discussed by Liu (2003), the observed amplitudes and inferred depth of discontinuities can be significantly affected by anelastic effects (absorption and dispersion) (e.g., Kanamori & Anderson, 1977). This is illustrated in Figure 4, which shows synthetic RF waveforms computed assuming different shear attenuation (Q_μ) models: a fully elastic medium (black), PREM reference model (blue), and two viscoelastic models (red and green) based on the extended Burgers model of Jackson and Faul (2010). Relatively small variations in shear attenuation model can result in non-negligible amplitude differences (e.g., blue and green models).

To account for anelastic effects, we rely on the extended Burgers viscoelastic model of Jackson and Faul (2010) and rheological parameters tabulated therein. This model is based on laboratory experiments of torsional forced-oscillation data on melt-free polycrystalline olivine. The main advantage of this model is that it can be directly linked with the thermodynamic computations as the latter provide the unrelaxed (infinite-frequency) shear modulus in addition to pressure and temperature (Khan et al., 2018). More specifically, shear attenuation as a function of depth for a given thermo-chemical model is derived from the shear modulus, temperature, and pressure profiles obtained by mineral phase equilibria calculations. In case the resultant shear attenuation values are larger than 600 (PREM crustal values), Q_μ is set equal to 600. This model thus allows us to self-consistently account for the influence of temperature and pressure on the shear attenuation model.

4.4. Influence of Temperature and Composition on RFs

In this section, we analyze the dependency of RF waveforms on thermal and compositional variations. To this end, we computed seismic properties for a range of basalt fractions and geotherms following the methodology described in section 2.1. The obtained properties were subsequently used to estimate synthetic RF waveforms as described in section 4.1 using the PREM (Dziewonski & Anderson, 1981) shear attenuation model. Figures 5a–5h summarize *S* wave velocity profiles and RF waveforms obtained using EA and MM models, respectively. Variations in phase proportions (modal mineralogy) for each thermo-chemical model are shown in the supporting information (Figures S3 and S4).

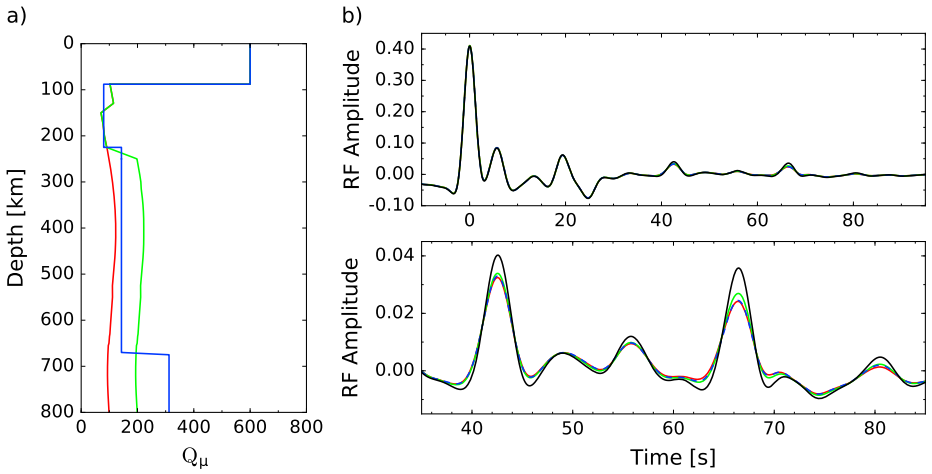

Figure 4. The effect of attenuation model on computed receiver functions (RF). (a) Shear attenuation models (Q_μ) correspond to: fully elastic medium (black), PREM reference model (blue), and two viscoelastic shear attenuation models (red and green) based on the rheological model of Jackson and Faul (2010). Note that the fully elastic model is not shown in panel (a) since $Q_\mu = \infty$. (b) Corresponding RF waveforms.

As reported in previous studies (e.g., Bina & Helffrich, 1994; Khan et al., 2009; Xu et al., 2008, among others), compositional and thermal variations affect the depth at which phase transitions occur as well as the amplitude and sharpness of the corresponding seismic discontinuity. For instance, Figure 5a shows that depth and amplitude of the 410-km seismic discontinuity decrease with increasing basalt fraction as the mode of $(Mg,Fe)_2SiO_4$-phases decreases (see the supporting information) and ultimately disappears for $f > 0.8$. Moreover, depth, amplitude, and sharpness of the 660-km discontinuity decrease with increasing basalt fraction due to the occurrence of bridgmanite and its decreasing mode at greater depth (see the supporting information), which simultaneously triggers the appearance of a discontinuity at ~800 km depth. Note that for $f > 0.5$, sharpness and amplitude of this new discontinuity significantly increase relative to those associated with the 660-km discontinuity. Furthermore, differences in velocity profiles computed using the EA (Figure 5a) and MM (Figure 5e) models are observed; for instance, MM velocity profiles are characterized by sharper velocity gradients in comparison to the EA model (for a detailed discussion see Xu et al., 2008).

Figures 5c and 5g depict the influence of thermal structure on V_s for the EA and MM models, respectively. Thermal variations have a larger effect on bulk velocities relative to compositional variations. Furthermore, the depth of the 410-km discontinuity significantly increases (from ~360 to ~440 km depth) with increasing temperature while the velocity jump remains almost constant. In contrast, the depth of the 660-km discontinuity decreases with increasing temperature while the sharpness of the discontinuity decreases due to an enrichment in majoritic garnet at higher temperatures (see the supporting information).

Figures 5b, 5d, 5f, and 5h illustrate how the aforementioned velocity variations affect amplitudes and travel times of *P*-to-*S* conversions occurring at 410- and 660-km seismic discontinuities and Figures 5i and 5j depict differential traveltime ($t_{P660s} - t_{textP410s}$) as a function of basalt fraction and temperature, respectively. The decrease in velocity jump and depth of the 410-km discontinuity associated with the increase in basalt fraction results in decreasing P410s amplitudes and earlier arrival times with increasing f (Figure 5b). Furthermore, the appearance of a second seismic discontinuity at ~800 km depth with increasing basalt fraction leads to changes in the P660s waveform from a single shallow peak ($f = 0$) to a single deep peak ($f = 1$) with a transition stage characterized by two distinct peaks.

Distinct 660 RF peaks have been reported in a number of regional and global studies (e.g., Ai et al., 2003; Andrews & Deuss, 2008; Maguire et al., 2018; Niu & Kawakatsu, 1996; Simmons & Gurrola, 2000; Tauzin et al., 2018). Additionally, differences between EA and MM models are also reflected in P410s and P660s waveforms. On the one hand, RF amplitudes for the MM model (Figure 5b) are slightly larger than the amplitudes estimated using the EA model (Figure 5f). Finally, the differential travel time increase with increasing basalt

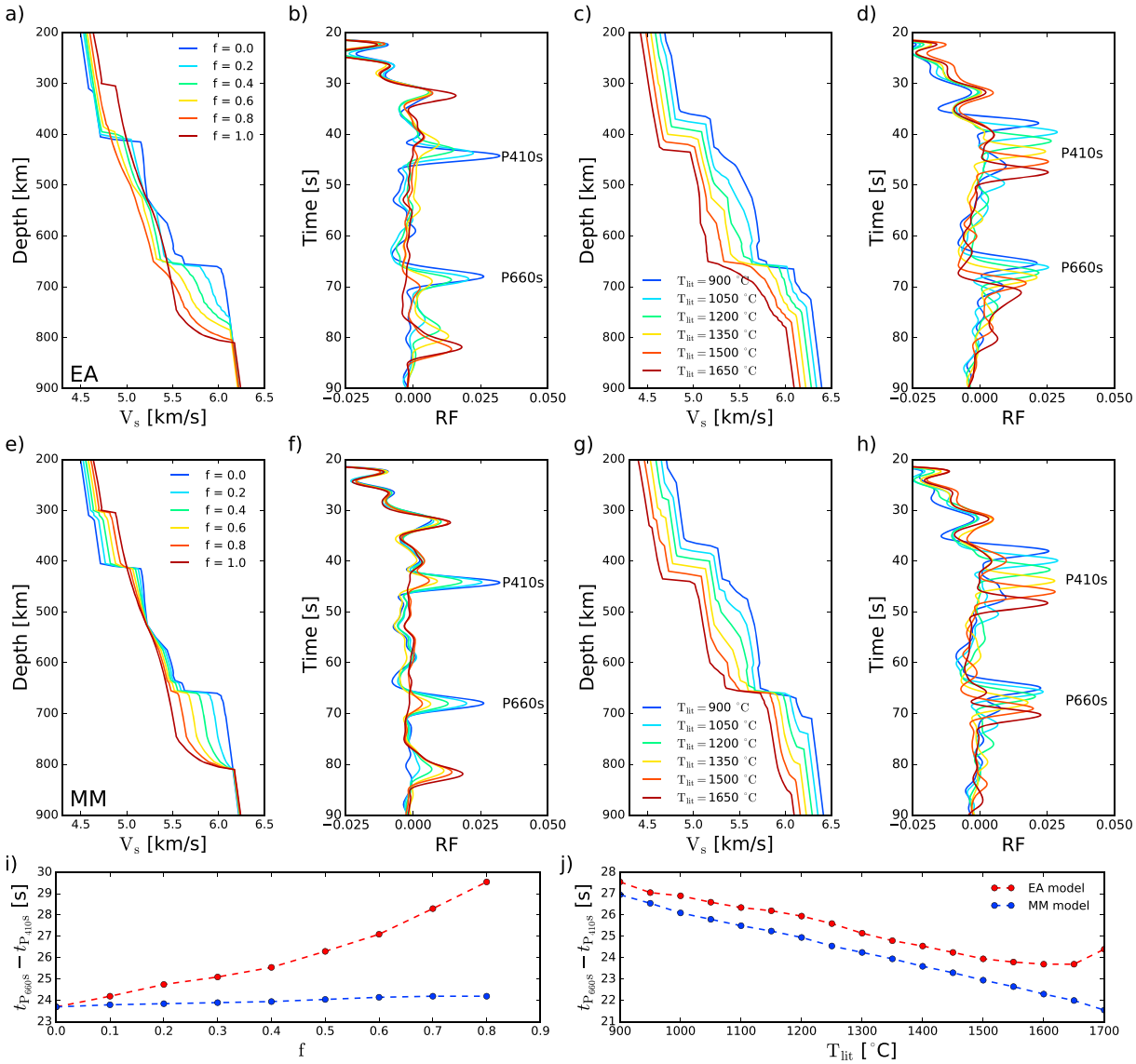

Figure 5. Shear-wave velocities (V_s) and receiver functions (RFs) as a function of mantle composition (f) and thermal structure (T_{lit}) for equilibrium assemblage (EA) and mechanical mixture (MM) mantle models. Velocity profiles as a function of basalt fraction f in (a) and (e) and the corresponding RF waveforms in (b) and (f) were computed assuming a sublithospheric adiabatic geotherm defined by the entropy of the lithology at a temperature T_{lit} of 1350 °C at the base of a 80-km-thick lithosphere. V_s profiles as a function of temperature in (c) and (g) and the associated RF waveforms shown in (d) and (h) were computed for fully equilibrated and mechanically mixed homogeneous pyrolitic (f = 0.2034) mantle models, respectively. Modal mineralogy associated with each thermo-chemical model is shown in the supporting information. Panels (i) and (j) depict differential travel times ($t_{P660s} - t_{P410s}$) as a function of basalt fraction and thermal structure, respectively. The differential travel times are tabulated in supporting information (Tables S1 and S2).

fraction for the EA model, whereas it is only weakly sensitive to compositional changes for the MM model (Figure 5i).

The influence of temperature on RF amplitude and travel time must be analyzed separately. Firstly, a linear increase in both P410s and P660s travel times is observed with increasing temperature (Figure 5d) due to a decrease in upper mantle velocities (Figure 5c). This typically results in the trade-off between the depth of an interface and upper mantle velocity seen in traditional approaches. Secondly, the decrease in TZ thickness as a function of temperature (Figure 5c) results in decreasing differential travel times with increasing temperature (Figure 5j). This decrease is linear for the MM model, whereas it is quasi-linear in the case of the EA model. Thirdly, P410s and P660s amplitudes depend nonlinearly on temperature due to variations in the sharpness of the seismic discontinuities (Figure 5h). The occurrence of phase changes associated with majoritic garnet

Table 2
Prior Information on Model Parameters and McMC Step Lengths

Description	# Parameter	Parameter	Range	Prior distribution	Step size
Crustal nodes	5	d_i	0–15 km	Uniform	4 km
Crustal velocities	1	V_s^1	2.75–5 km/s	Uniform	0.10 km/s
	4	V_s^i	V_s^{i-1}–5 km/s	Uniform	0.10 km/s
Lithospheric thickness	1	z_{lit}	60–250 km	Uniform	10 km
Temperature at z_{lit}	1	T_{lit}	800–1700 °C	Uniform	15° C
Basalt fraction	1	f	0–0.7	Uniform	0.05

and ferropericlase (see the supporting information) adds additional complexity to the TZ response. Hence, to avoid the pitfalls arising from the use of travel times of converted waves only, including the Clapeyron slope of $(Mg,Fe)_2SiO_4$-phases, all phase changes need to be considered to infer mantle temperatures properly. As a consequence, we use the entire RF waveform to map thermo-chemical variations in Earth's mantle. This allows for joint recovery of crust and mantle structure, while doing away with the need for tomographic models to correct for crust and upper mantle effects.

Finally, bulk velocities are seen to affect the long-period content of RF waveforms. In particular, the long-period behavior seems relatively stable in the case of changes in basalt fraction (Figures 5a, 5b, 5e, and 5f) leading to only small variations in bulk *S* wave velocities within the mantle TZ. In contrast, temperature variations trigger long-period changes in the RF waveform, especially for the EA model (Figures 5d and 5h). This behavior can be attributed to changes in the large-scale vertical velocity gradient and suggests that very long-period waveforms may be suitable for constraining mantle velocity structure.

5. Inverse Problem

To infer TZ thermal and compositional structure, we invert the observed RF waveforms using the model parameterization and the forward operator described previously (sections 2 and 4). Deterministic derivative-based methods, such as Gauss-Newton, can be applied, but these methods typically depend on the choice of initial model and converge to a local minimum. To overcome these limitations and the non-uniqueness of RF inversion (Ammon et al., 1990; Jacobsen & Svenningsen, 2008), we combine a McMC (Tarantola, 2005) method with a stochastic optimization technique known as Covariance Matrix Adaptation Evolution Strategy (CMAES; Hansen & Ostermeier, 2001).

5.1. CMAES

This technique aims to explore the model space globally showing remarkable robustness on ill-conditioned problems (Hansen et al., 2011). The use of CMAES in geophysics is not common, but has recently been implemented as a global minimization method (Alvers et al., 2013; Diouane, 2014; Grayver et al., 2016; Munch et al., 2018; Shen et al., 2015) outperforming other optimization techniques such as Genetic Algorithms and Particle Swarm Optimization (Arsenault et al., 2013; Auger et al., 2009; Elshall et al., 2015).

We employ CMAES for finding the maximum a-posteriori model $\mathbf{m}_{MAP}$ by solving the following optimization problem

$$\mathbf{m}_{MAP} = \underset{\mathbf{m}}{\operatorname{argmin}} \left(\sum_{i=1}^{N_w} \phi_i(\mathbf{m}) \right) \quad \text{with} \quad \phi_i(\mathbf{m}) = \frac{1}{N_i} \sum_{j=1}^{N_i} \left[\frac{RF^{obs}(t_j) - RF^{mod}(\mathbf{m}, t_j)}{\delta RF^{obs}(t_j)} \right]^2, \tag{3}$$

where N_w is the number of time windows of interest (see section 6.2) and N_i is the number of samples in each time window; RF^{mod} indicates modeled RF waveform, whereas RF^{obs} denotes observed RF waveform with uncertainties δRF^{obs} (see section 3). Vector $\mathbf{m} = (T_{lit}, z_{lit}, f, V_s^1, \dots, V_s^5, d_1, \dots, d_5)$ contains the various model parameters described previously (sections 2.1 and 2.2). Table 2 summarizes model parameters and model parameters search ranges used in the inversions.

At every iteration the algorithm samples λ models from the current multivariate normal distribution and evaluates the misfit between observed and synthetic data. Then the best $\lambda/2$ candidates are selected and used to update the distribution mean, step size, and covariance matrix (Grayver & Kuvshinov, 2016). Following Hansen

and Ostermeier (2001), a reasonable choice for the number of sampled models is given by $\lambda = 4 + 3\,\lfloor \ln M \rfloor$; where $\lfloor \cdot \rfloor$ is the floor function and M is the number of unknowns. This equation was used to choose the population size λ in all inversions. Finally, we considered different initial models and number of iterations N_{max} (25–400), but generally, solutions were found to be equivalent for $N_{max} > 100$.

5.2. McMC

We solve the nonlinear inverse problem within a Bayesian framework using the probabilistic approach of Tarantola and Valette (1982). In this formulation, the solution to the inverse problem is described in terms of the posterior probability distribution $\sigma(\mathbf{m})$ given by (Mosegaard & Tarantola, 1995)

$$\sigma(\mathbf{m}) = k\rho(\mathbf{m})\mathcal{L}(\mathbf{m}), \tag{4}$$

where k is a normalization constant, $\rho(\mathbf{m})$ is a probability distribution that describes the a priori information on model parameters (summarized in Table 2), and the likelihood function $\mathcal{L}(\mathbf{m})$ represents a measure of the similarity between the observed data and the predictions from model $\mathbf{m}$. Under the assumption that noise can be modeled using a Gaussian distribution, the likelihood function is given by (Tarantola, 2005)

$$\mathcal{L}(\mathbf{m}) \propto \exp\left(-\frac{1}{2}\sum_{i=1}^{N_w}\phi_i(\mathbf{m})\right) \tag{5}$$

where N_w is the number of time windows of interest and $\phi_i(\mathbf{m})$ is the misfit between observed and modeled data as defined by equation (3).

We employ the Metropolis-Hastings (Hastings, 1970; Metropolis et al., 1953) algorithm to sample the posterior distribution in the model space using the solution retrieved from the CMAES algorithm $\mathbf{m}_{MAP}$ as initial model. This considerably improves the efficiency of the McMC method by significantly reducing the burn-in period (Grayver & Kuvshinov, 2016). To further improve the efficiency of the McMC stage, the sampling is performed using 10 independent chains (with a total length of 10,000 iterations) characterized by identical initial models but different randomly chosen initial perturbations. This strategy allows for sampling 100,000 models with moderate computational cost (~5 days using 10 cores). Finally, the 50,000 best-fitting candidates are used to build histograms of the marginal probability distribution of each model parameter.

6. Results

6.1. Synthetic Inversion

In order to test the robustness of our inverse scheme, we performed different sets of synthetic inversions. To this end, a synthetic stack was computed for a homogeneous pyrolitic mantle ($f = 0.2034$), a temperature T_{lit} of 1350°C at the base of a 150-km-thick lithosphere, and crustal structure fixed to IASP91 (Kennett & Engdahl, 1991). The computed stack was then contaminated with 7% Gaussian noise filtered in the frequency band 0.01–0.2 Hz. Finally, the resulting synthetic RF waveform was inverted to retrieve (1) the thermo-chemical parameters, that is, T_{lit}, z_{lit}, f assuming a known crustal structure and (2) both thermo-chemical and crustal parameters.

Figure 6 summarizes the main inversion results for mantle thermo-chemical parameters for the case where crustal structure is fixed to IASP91 (true solution) and an arbitrary choice of starting model. Figure 6a depicts root-mean-square error (RMSE) surfaces estimated by grid search exploration of the model space. Green dots represent the true solution and magenta dots indicate the best-fitting model candidate at each iteration of the CMAES evolution from starting model (red triangles) to the final model (blue star). Figure 6b shows histograms of marginal probability distributions for each model parameter built from the 50,000 best-fitting models sampled by the McMC method. As shown in Figure 6c, model parameters retrieved by CMAES algorithm (blue) and McMC sampled models (green) fit the data (black) within uncertainties (dashed lines). Visual inspection of the RMSE surfaces reveals a positive correlation between z_{lit} and T_{lit} and the existence of a local minimum. Despite the nonlinearity of the problem, CMAES succeeds in finding the global minimum. In the case of basalt fraction f, the CMAES solution is almost coincidental with the true model, whereas final values of T_{lit} and z_{lit} are slightly shifted with respect to the true solution. These small differences are attributed to the presence of noise in the data. Finally, sampled probability distributions provide uncertainties on the recovered model parameters ($\delta T_{lit} \sim 40$°C, $\delta z_{lit} \sim 25$km , and $\delta f \sim 0.05$). Furthermore, the histogram for z_{lit} is broader suggesting a lack of sensitivity to this particular parameter. Sensitivity in the upper mantle can be increased by incorporating additional information from other geophysical techniques such as surface wave

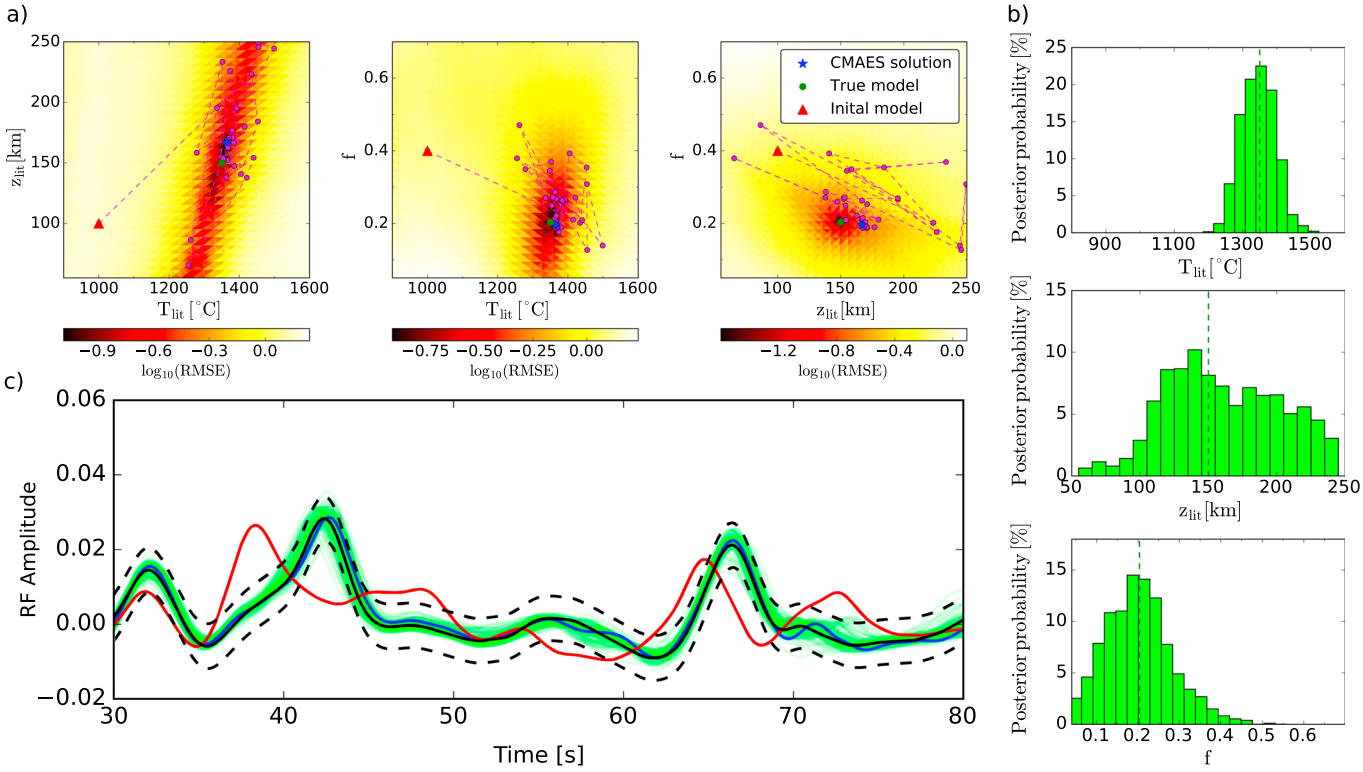

Figure 6. Inversion of synthetic receiver functions (RF) for thermo-chemical parameters with fixed crustal structure (IASP91). (a) Root-mean-square error (RMSE) surfaces obtained by grid search exploration of the model space considering 30 points in each direction. Green dots, red triangles, and blue stars indicate the positions of true, initial, and final models, respectively. Magenta dots depict best-fitting solutions retrieved from the Covariance Matrix Adaptation Evolution Strategy (CMAES) at each iteration. (b) Histograms showing thermo-chemical parameters sampled by Markov chain Monte Carlo (McMC) exploration of the model space around the CMAES final solution. Vertical dashed lines indicate true model parameters. (c) Comparison between synthetic RF waveforms for the initial (red), CMAES (blue), and true (black) solutions. Green lines depict McMC sampled RF waveforms. Dashed lines indicate data uncertainties.

group and phase velocities (e.g., Bodin et al., 2012; Calò et al., 2016; Khan et al., 2009; Shan et al., 2014) or *S*-to-*P* conversions (e.g., Oreshin et al., 2008; Yuan et al., 2006).

In order to analyze the influence of unaccounted-for crustal structure on the retrieval of mantle thermo-chemical parameters, we performed a set of synthetic inversions using different crustal models. More specifically, we increased crustal velocities by 20% (*model A*) and Moho depth by 10 km (*model B*) from the true solution (IASP91). Figure 7a depicts best-fitting basalt fractions f, adiabatic geotherms (left panel), and the corresponding *S* wave velocity profiles (right panel) retrieved for each crustal model. Figure 7b shows the fits between observed (black) and computed RF waveforms. Although P410s and P660s are explained within uncertainties, significant differences are observed in the time window $-5\,\mathrm{s} < t < 25\,\mathrm{s}$. The amplitude of the P-arrival as well as time and amplitude of the multiples significantly depend on the assumed crustal structure. As shown in Figure 7a, differences in the crustal model are seen to significantly affect the retrieval of mantle thermo-chemical parameters (ΔT_{lit} ~50 °C, Δz_{lit} ~50 km, and Δf ~0.1). This synthetic test illustrates the importance of accurately accounting for crustal structure when inverting for the TZ structure.

6.2. Accounting for Crustal Structure

In light of the aforementioned results, an accurate characterization of the shallow structure beneath each station is essential. As a result, we propose an inverse strategy that allows simultaneous recovery of crust and mantle structure. Our strategy consists of two steps: in step 1, we invert the observed RF waveform in the time window $-5\,\mathrm{s} < t < 25\,\mathrm{s}$ for crustal structure (leaving mantle parameters variable), followed by a second inversion (step 2) of the entire observed RF waveform in the time windows $-5\,\mathrm{s} < t < 25\,\mathrm{s}, 36\,\mathrm{s} < t < 50\,\mathrm{s}$, and $60\,\mathrm{s} < t < 80\,\mathrm{s}$ to recover both crustal and mantle thermochemical parameters with the model obtained from step 1 as input. We tested different time windows in which observations are fitted. The final choice of specific time windows is somewhat arbitrary, but time windows containing considerably small or no signal can introduce undesirable noise into the misfit function and unnecessarily increase the complexity of the misfit surface.

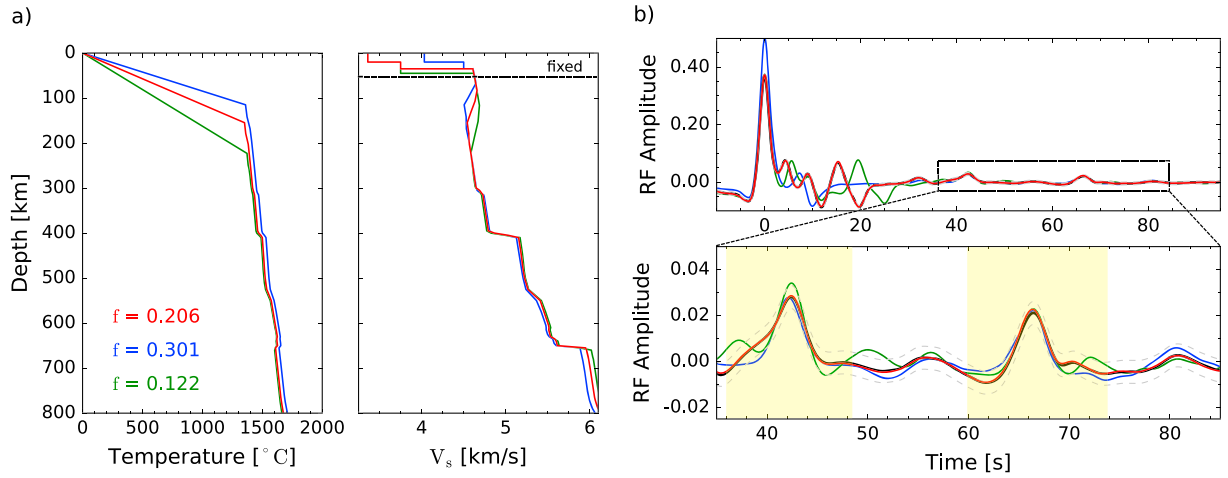

Figure 7. Single-step inversion of synthetic receiver functions (RF) for thermo-chemical parameters fixing crustal structure to three different crustal models (see detailed model description in section 6.1): IASP91 (red), *model A* (blue), and *model B* (green). Panel (a) depicts best-fitting basalt fractions f and thermal structures (left) and corresponding *S* wave velocity V_s as a function of depth (right). Panel (b) shows datafit between observed (black) and computed RF waveforms, given the data uncertainties indicated by gray dashed lines. Yellow rectangles indicate the part of the RF waveform that is fitted in the inversion.

Figure 8 illustrates the performance of the proposed two-step inversion strategy. The method succeeds in recovering the true thermal structure and basalt fraction, however, intra-crustal discontinuities are not well resolved. This can be explained by the fact that the proposed methodology mainly focuses on the recovery of mantle thermo-chemical structure and, thus, only an effective crustal structure that explains correctly the long-period waveforms (below 0.2 Hz) is retrieved. Higher frequency content (up to 1 Hz) should be included to increase the resolution in the crust. Future work will focus on incorporating the use of high frequency RF waveforms into our two-step procedure for better reconstructing crustal structure. Synthetic tests (not shown here) indicate that the use of the recovered model from step 1 as input model significantly improves the performance of the algorithm in finding the global minimum.

The synthetic tests presented above were performed using the same model parameterization to solve both forward and inverse problems. As an independent test, we computed a synthetic stacked RF waveform using the IASP91 velocity model (Kennett & Engdahl, 1991) and subsequently inverted it for crustal and mantle parameters. The main results are shown in Supporting Information (Figure S5). Both EA and MM models

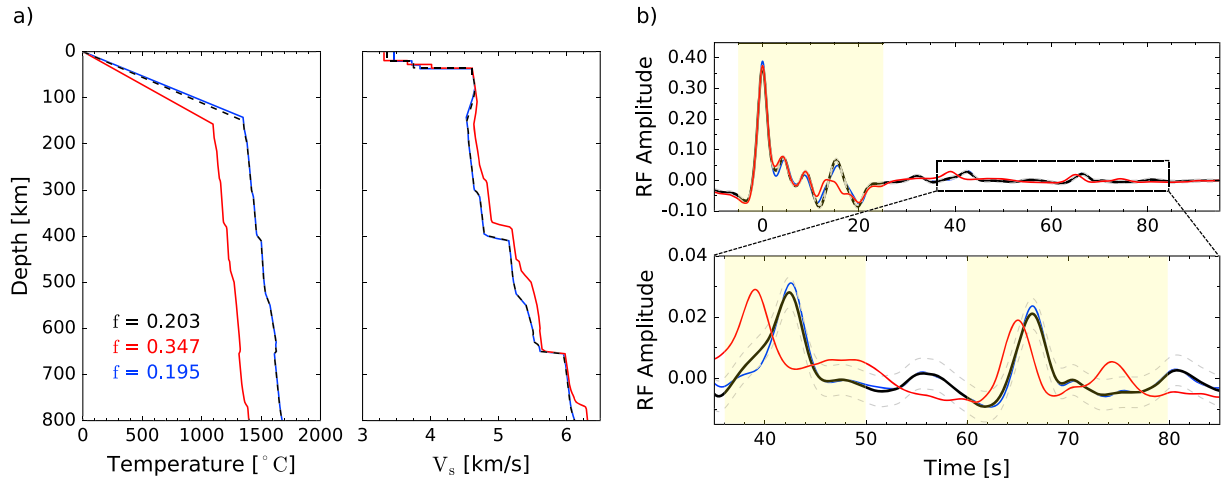

Figure 8. Two-step inversion of synthetic receiver functions (RF) for crustal and thermo-chemical parameters. Panel (a) depicts best-fitting basalt fraction f and thermal structure (left panel) and corresponding *S* wave velocity V_s (right panel). Panel (b) shows fit between observed (black) and computed RF waveforms with yellow rectangles indicating time windows fitted in the inversion. Black curves correspond to the true model, red curves denote best-fitting model obtained by inverting the early part of the RF waveform (step 1 $-5\ s < t < 25\ s$), and blue curves indicate best-fitting solution from inversion of the entire RF waveform (step 2).

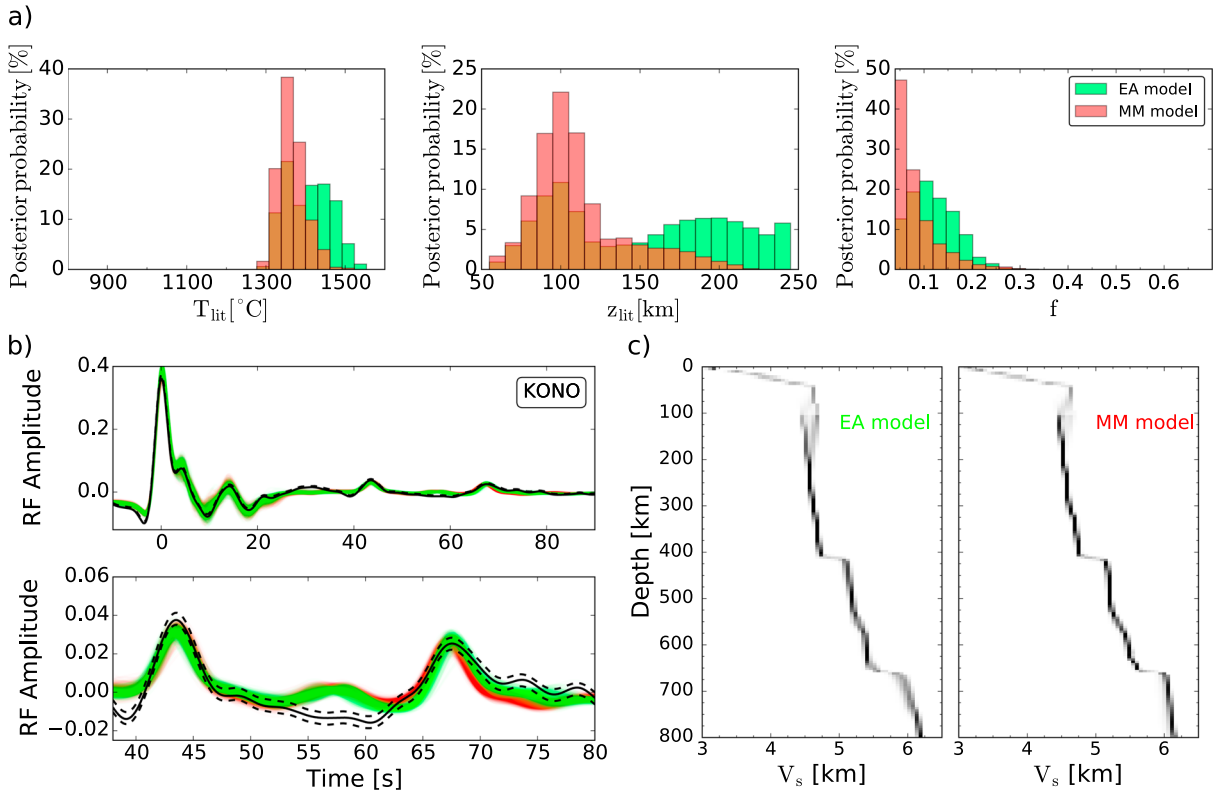

Figure 9. Inversion results for Kongsberg (KONO) station. Panel (a) depicts sampled mantle thermo-chemical parameters for the equilibrium assemblage (EA) and mechanical mixture (MM) mantle models, respectively. Orange-colored binds indicate model parameters for which EA and MM overlap. Panel (b) shows fit between observed (black) and synthetic receiver function (RF) waveforms for the MM (red) and EA (green) mantle models. Data uncertainties are indicated by black dashed lines. Panel (c) depicts sampled *S* wave velocity (V_s) profiles for the EA and MM models with black indicating most probable and white least probable.

explain the observed RF waveform with almost identical mantle thermo-chemical parameters. The recovered seismic profiles above the 410-km discontinuity are in reasonable agreement but show larger jumps at the 410-km discontinuity and lower TZ gradients. Finally, inferred Moho depth and absolute velocity in the first layer are in agreement with the true solution, although, intracrustal discontinuities are not well resolved.

6.3. Data Examples

As a proof of concept, we apply the proposed methodology to infer mantle composition and thermal structure beneath two permanent stations (see Figure 2a) located in two distinct stable continental regions: Kongsberg (KONO) in the East European craton and Yakutsk (YAK) in the Siberian craton. Observed stacks and uncertainty estimates (Figure 2c) were obtained by applying the data processing scheme detailed in section 3.

Figures 9 and 10 summarize the main results obtained for KONO and YAK, respectively. Panels (a) show sampled marginal probability distributions of mantle thermo-chemical parameters retrieved for the EA and MM mantle models; panels (b) depict the fit between observed (black) and synthetic RF waveforms for the MM (red) and EA (green) mantle models; and panels (c) show sampled *S* wave velocity profiles. Mantle thermal profiles and the associated shear attenuation models are depicted in supporting information (Figure S6).

All retrieved models succeed at explaining the observed P410s (40 s $< t <$ 50 s) and P660s (65 s $< t <$ 71 s) waveforms within uncertainties as well as the amplitude of the *P* arrival (−2 s $< t <$ 2 s) and main crustal reverberations (5 s $< t <$ 25 s). The models also predict a positive pulse in the RF waveforms (50 s $< t <$ 60 s) associated with the wadsleyite→ringwoodite transition. Such a feature is not present in the observed RF waveforms for KONO, while it is partially observed for YAK. This difference can possibly be attributed to multiples originating from reflections atop sharp mid-lithospheric/cratonic discontinuities (e.g., Calò et al., 2016; Rychert & Shearer, 2009) which can potentially mask weak *P*-to-*S* conversions occurring within the mantle TZ. Alternatively, the wadsleyite→ringwoodite transition could be the result of the long-period behavior of RF waveforms, which depends on the large-scale velocity gradient across the mantle TZ (see section 4.4).

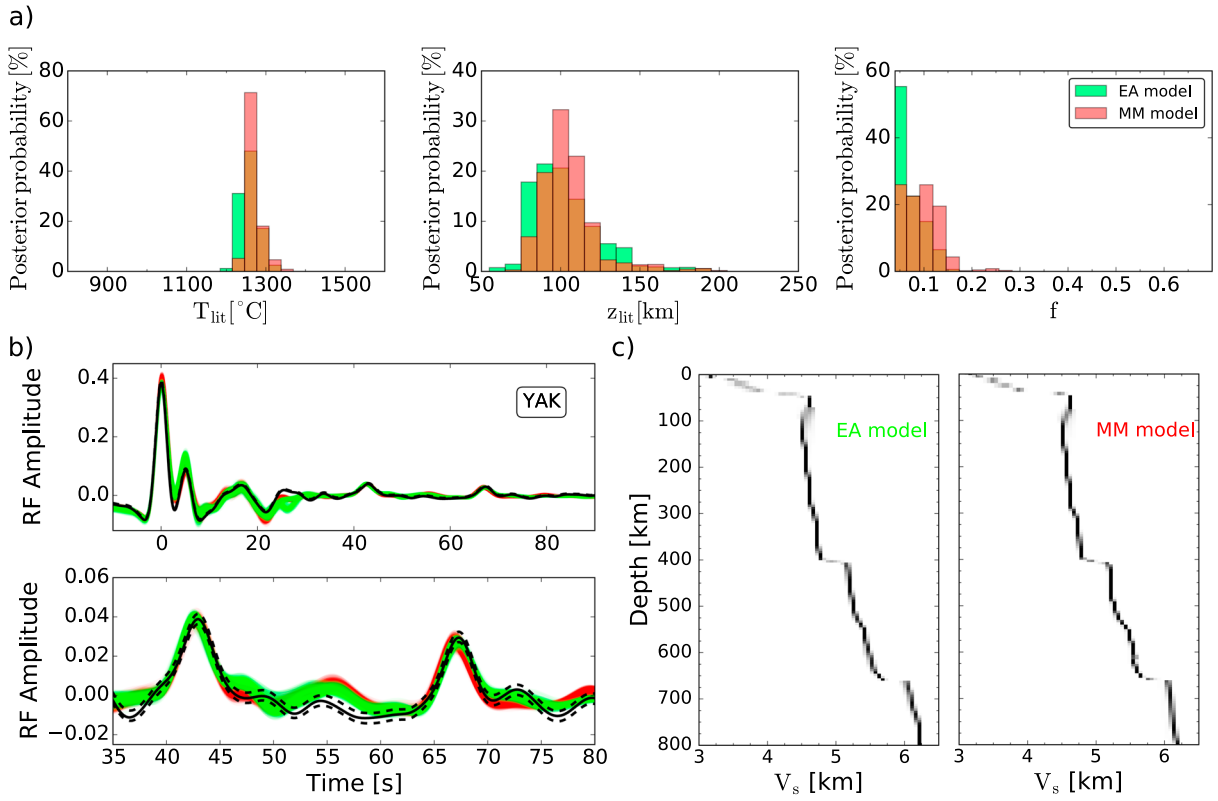

Figure 10. Inversion results for Yakutsk (YAK) station. Panel (a) depicts sampled mantle thermo-chemical parameters for the equilibrium assemblage (EA) and mechanical mixture (MM) mantle models, respectively. Orange-colored binds indicate model parameters for which EA and MM overlap. Panel (b) shows fit between observed (black) and synthetic receiver function (RF) waveforms for the MM (red) and EA (green) mantle models. Data uncertainties are indicated by black dashed lines. Panel (c) depicts sampled *S* wave velocity (V_s) profiles for the EA and MM models with black indicating most probable and white least probable.

While the results generally tend to agree between the EA and MM models, subtle differences are palpable. For instance, marginally more harzburgite-enriched compositions are obtained for KONO (see Figure 9a) for the MM model relative to the EA model. Thermal parameters inferred for KONO (EA) are characterized by a broader distribution, whereas a relatively well-defined distribution is recovered for the MM model. Despite this difference, most probable T_{lit} and z_{lit} estimates are equivalent for both EA and MM. This contrasts with what was reported by Ritsema, Xu, et al. (2009) where the EA model was found to result in higher temperature estimates relative to MM. This discrepancy can be explained by the fact that Ritsema, Xu, et al. (2009) neglect compositional effects and only considers a pyrolitic mantle composition. To further distinguish between EA and MM models, additional sources of information should be considered such as temperature estimates from olivine thermometry (e.g., Ritsema, Xu, et al., 2009).

Thermal parameters T_{lit} and z_{lit} inferred for YAK and KONO correspond to potential temperature estimates of 1230 ± 30 °C and 1280 ± 35 °C, respectively. These estimates are slightly lower than experimentally determined mantle potential temperature estimates (1330 ± 40 °C) by Katsura et al. (2010). This discrepancy can also be attributed to the fact that Katsura et al. (2010) focus on a pyrolitic mantle composition. Moho depths inferred beneath KONO (~34 km) and YAK (~40 km) are in agreement with estimates (~35 km and ~42 km, respectively) from the regional crustal models EUNAseis (Artemieva & Thybo, 2013) and SibCrust (Cherepanova et al., 2013), respectively. These crustal models represent compilations of European and Siberian regional and local seismic models derived from controlled source and RF studies.

7. Discussion

First off, we performed waveform modeling in a homogeneous and radially stratified isotropically layered model. Consequently, this approach is unable to account for material anisotropy and diffraction effects related to three-dimensional mantle structure. In spite of stacking waveforms that sense the equivalent of a circular

area exceeding 250 km in radius (at 660 km depth) beneath the station (see Figure 2 in Tauzin et al., 2008), it is possible that these assumptions introduce errors into the recovered model. To obtain a better sense of the errors, wave propagation simulations based on more advanced waveform modeling schemes should be considered (e.g., Monteiller et al., 2012; Nissen-Meyer et al., 2014).

Second, the noise model considered in the synthetic examples (section 6.1) does not account for noise due to incoherent stacking. As a quantitative description of this effect is challenging, we discuss the errors that could potentially be introduced hereby. Incoherent stacking could broaden and decrease the amplitude of converted waves. As a result, broader and smaller velocity gradients would be required to explain these waveforms. Given the influence of temperature and composition on RF waveforms (section 4.4), the recovered thermo-chemical parameters would be biased in favour of more basalt-enriched compositions and higher temperature estimates.

Third, the thermo-chemical parameterization (uniform adiabatic mantle) is technically limited to geotectonic settings representative of "normal" mantle conditions and will need to be modified to encompass subduction zones and other more complex geological settings. While reliance on basalt and harzburgite as end-members to model mantle composition presents a practical first-order approximation from a geophysical point of view, more complicated models can be built by incorporating other plausible end-members such as lherzolitic and dunitic compositions. Although CFMASNa-equivalent basaltic and harzburgitic end-member compositions are nonunique (cf. Brown & Mussett, 1993; Henderson & Henderson, 2009; Khan et al., 2009; Xu et al., 2008), its influence on geodynamic models has been shown to be significant only for FeO and Al_2O_3 contents (Nakagawa et al., 2010). Finally, the viscoelastic model of Jackson and Faul (2010) employed here only considers the viscoelastic behavior of olivine. Future studies, based on expanded experimental data, should consider the importance of other minerals in more detail.

In spite of these caveats, it is our contention that the methodology outlined here is capable of making significant quantitative predictions and presents several advantages with respect to classical inversion of RF waveforms: it anchors temperature, composition, and seismic discontinuities that are in laboratory-based data and models, while simultaneously permitting the use of geophysical inverse methods to optimize profiles of physical properties (e.g., bulk and shear modulus and density) to match RF waveforms. As a result, depth and sharpness of 410- and 660-km discontinuities are determined self-consistently from composition, temperature, and pressure. In contrast to studies relying on RF migration, estimates of TZ topography and volumetric velocities derived here are independent of global/regional tomographic models and, finally, assumptions about Clayperon slopes for interpretation of TZ thermal structure are obviated.

8. Concluding Remarks and Outlook

We presented a methodology for stochastic inversion of *P*-to-*S* converted waves to directly infer variations in mantle temperature and composition. To this end, we employ self-consistent mineral phase equilibria calculations to estimate mantle elastic properties as a function of pressure, temperature, and composition. Two end-member compositional models for mixing harzburgite and basalt were considered: the completely equilibrated Equilibrium Assemblage (EA) model and the disequilibrated Mechanical Mixture (MM) model.

We first analyzed the effect of thermal and compositional variations on RFs. The former was found to influence arrival times, whereas the latter affected the amplitude of waves converted at the discontinuities that bound the TZ. Based on this, we proceeded to consider interpretation of RF waveforms as an inverse problem with the goal of determining mantle thermo-chemical and crustal structure by interfacing the geophysical analysis with phase equilibria computations. During the inversion, the slowness distribution recorded at each station must be accurately replicated and identical methods should be applied to both observed and synthetic seismograms. The robustness of our inverse strategy was tested by performing a set of synthetic inversions in which crustal structure was assumed both fixed and variable. This analysis indicated that unaccounted-for crustal structure strongly affects the retrieval of mantle structure. Therefore, an accurate characterization of crustal structure beneath a given station is needed. To properly account for the influence of the crust, we first inverted for crustal structure, then used this model as input, and finally inverted for both crust and mantle structure.

As a proof of concept, we applied the proposed methodology to data from two permanent stations located in two distinct stable continental regions: Yakutsk on the Siberian craton and Kongsberg on the East

European craton. The retrieved models based on both EA and MM succeeded in explaining the main features of the observed RF waveforms within uncertainties with only minor differences in the retrieved candidates: the MM model leads to marginally more harzburgite-enriched compositions beneath Kongsberg. To further distinguish between the two models, petrological constraints (e.g., olivine thermometry) should be incorporated (e.g., Afonso et al., 2016; Ritsema, Xu, et al., 2009).

Future improvements will include (1) inversion of RF waveforms in multiple frequency bands (e.g., Schmandt, 2012) and jointly with surface wave data (e.g., Calò et al., 2016), (2) consideration of a depth-dependent composition, and (3) exploring deviations from an adiabatic profile. This will be needed to improve resolution in the upper mantle and the TZ, to address convection simulations that suggest the existence of local compositional gradients across the mantle (e.g., Ballmer et al., 2015), and to enable us to consider regions or features that deviate from "normal" mantle conditions (e.g., stagnant slabs).

Acknowledgments
We are grateful to Erik Duesterhoeft and two anonymous reviewers for comments that led to an improved manuscript. The authors would also like to thank George Helffrich for input at the early stage of this study. This work was supported by a grant from the Swiss National Science Foundation (SNF project 200021_159907). B. T. was funded by a Délégation CNRS and Congé pour Recherches et Conversion Thématique from the Université de Lyon to visit the Research School of Earth Sciences (RSES), The Australian National University (ANU). B. T. has received funding from the European Union's Horizon 2020 research and innovation programme under the Marie Sklodowska-Curie grant agreement 793824. The IRIS Data Management Center (http://ds.iris.edu/SeismiQuery/channel.htm) was used for access to waveforms of stations YAK and KONO. IRIS Data Services are funded through the Seismological Facilities for the Advancement of Geoscience and EarthScope (SAGE) Proposal of the National Science Foundation under cooperative agreement EAR-1261681.

References

Afonso, J., Fullea, J., Yang, Y., Connolly, J., & Jones, A. (2013). 3-D multi-observable probabilistic inversion for the compositional and thermal structure of the lithosphere and upper mantle. II: General methodology and resolution analysis. *Journal of Geophysical Research: Solid Earth*, *118*, 1650–1676. https://doi.org/10.1002/jgrb.50123

Afonso, J. C., Rawlinson, N., Yang, Y., Schutt, D. L., Jones, A. G., Fullea, J., & Griffin, W. L. (2016). 3-D multiobservable probabilistic inversion for the compositional and thermal structure of the lithosphere and upper mantle: III. Thermochemical tomography in the Western-Central US. *Journal of Geophysical Research: Solid Earth*, *121*, 7337–7370. https://doi.org/10.1002/2016JB013049

Ai, Y., Zheng, T., Xu, W., He, Y., & Dong, D. (2003). A complex 660 km discontinuity beneath northeast China. *Earth and Planetary Science Letters*, *212*(1-2), 63–71.

Aki, K., & Richards, P. G. (2002). *Quantitative seismology*. CA: University Science Books.

Alvers, M., Götze, H., Lahmeyer, B., Plonka, C., & Schmidt, S. (2013). Advances in 3D potential field modeling. In *75Th EAGE Conference Andamp; Exhibition Incorporating SPE EUROPEC 2013*.

Ammon, C. J., Randall, G. E., & Zandt, G. (1990). On the nonuniqueness of receiver function inversions. *Journal of Geophysical Research*, *95*(B10), 15,303–15,318.

Andrews, J., & Deuss, A. (2008). Detailed nature of the 660 km region of the mantle from global receiver function data. *Journal of Geophysical Research*, *113*, B06304. https://doi.org/10.1029/2007JB005111

Arsenault, R., Poulin, A., Côté, P., & Brissette, F. (2013). Comparison of stochastic optimization algorithms in hydrological model calibration. *Journal of Hydrologic Engineering*, *19*(7), 1374–1384.

Artemieva, I. M., & Thybo, H. (2013). EUNAseis: A seismic model for Moho and crustal structure in Europe, Greenland, and the North Atlantic region. *Tectonophysics*, *609*, 97–153.

Auger, A., Hansen, N., Zerpa, J. M. P., Ros, R., & Schoenauer, M. (2009). Experimental comparisons of derivative free optimization algorithms. *SEA*, *5526*, 3–15.

Ballmer, M. D., Schmerr, N. C., Nakagawa, T., & Ritsema, J. (2015). Compositional mantle layering revealed by slab stagnation at ~1000-km depth. *Science Advances*, *1*(11), e1500815.

Bass, J. D. (1995). Elasticity of minerals, glasses, and melts. In T. J. Ahrens (Ed.), *Mineral physics & crystallography: A handbook of physical constants* (pp. 45–63). Washington, DC: American Geophysical Union.

Bentham, H., & Rost, S. (2014). Scattering beneath western pacific subduction zones: Evidence for oceanic crust in the mid-mantle. *Geophysical Journal International*, *197*(3), 1627–1641.

Bercovici, D., & Karato, S.-I. (2003). Whole-mantle convection and the transition-zone water filter. *Nature*, *425*(6953), 39–44.

Bina, C. R., & Helffrich, G. (1994). Phase transition Clapeyron slopes and transition zone seismic discontinuity topography. *Journal of Geophysical Research*, *99*(B8), 15,853–15,860.

Bodin, T., Sambridge, M., Tkalčić, H., Arroucau, P., Gallagher, K., & Rawlinson, N. (2012). Transdimensional inversion of receiver functions and surface wave dispersion. *Journal of Geophysical Research*, *117*, B02301. https://doi.org/10.1029/2011JB008560

Brandenburg, J. P., & van Keken, P. E. (2007). Deep storage of oceanic crust in a vigorously convecting mantle. *Journal of Geophysical Research*, *112*, B06403. https://doi.org/10.1029/2006JB004813

Brown, G. C., & Mussett, A. E. (1993). *The inaccessible Earth: An integrated view to its structure and composition*. Netherlands: Springer.

Calò, M., Bodin, T., & Romanowicz, B. (2016). Layered structure in the upper mantle across North America from joint inversion of long and short period seismic data. *Earth and Planetary Science Letters*, *449*, 164–175.

Cammarano, F., Deuss, A., Goes, S., & Giardini, D. (2005). One-dimensional physical reference models for the upper mantle and transition zone: Combining seismic and mineral physics constraints. *Journal of Geophysical Research*, *110*, B01306.

Cao, A., & Levander, A. (2010). High-resolution transition zone structures of the Gorda Slab beneath the western United States: Implication for deep water subduction. *Journal of Geophysical Research*, *115*, B07301. https://doi.org/10.1029/2009JB006876

Chang, Y.-Y., Jacobsen, S. D., Bina, C. R., Thomas, S.-M., Smyth, J. R., Frost, D. J., et al. (2015). Comparative compressibility of hydrous wadsleyite and ringwoodite: Effect of h_2O and implications for detecting water in the transition zone. *Journal of Geophysical Research: Solid Earth*, *120*, 8259–8280. https://doi.org/10.1002/2015JB012123

Chen, L., & Ai, Y. (2009). Discontinuity structure of the mantle transition zone beneath the North China Craton from receiver function migration. *Journal of Geophysical Research*, *114*, B06307. https://doi.org/10.1029/2008JB006221

Chen, C.-Y., Frey, F., Garcia, M., Dalrymple, G., & Hart, S. (1991). The tholeiite to alkalic basalt transition at Haleakala Volcano, Maui, Hawaii. *Contributions to Mineralogy and Petrology*, *106*(2), 183–200.

Cherepanova, Y., Artemieva, I. M., Thybo, H., & Chemia, Z. (2013). Crustal structure of the Siberian craton and the West Siberian basin: An appraisal of existing seismic data. *Tectonophysics*, *609*, 154–183.

Chevrot, S., Vinnik, L., & Montagner, J.-P. (1999). Global-scale analysis of the mantle PDS phases. *Journal of Geophysical Research*, *104*(B9), 20,203–20,219.

Chust, T., Steinle-Neumann, G., Dolejš, D., Schuberth, B., & Bunge, H.-P. (2017). MMA-eoS: A computational framework for mineralogical thermodynamics. *Journal of Geophysical Research: Solid Earth*, *122*, 9881–9920. https://doi.org/10.1002/2017JB014501

Cline, C. II, Faul, U., David, E., Berry, A., & Jackson, I. (2018). Redox-influenced seismic properties of upper-mantle olivine. *Nature*, *555*(7696), 355–358.
Cobden, L., Goes, S., Cammarano, F., & Connolly, J. A. (2008). Thermochemical interpretation of one-dimensional seismic reference models for the upper mantle: Evidence for bias due to heterogeneity. *Geophysical Journal International*, *175*(2), 627–648.
Connolly, J. (2009). The geodynamic equation of state: What and how. *Geochemistry, Geophysics, Geosystems*, *10*, Q10014. https://doi.org/10.1029/2009GC002540
Connolly, J., & Khan, A. (2016). Uncertainty of mantle geophysical properties computed from phase equilibrium models. *Geophysical Research Letters*, *43*, 5026–5034. https://doi.org/10.1002/2016GL068239
Cottaar, S., & Deuss, A. (2016). Large-scale mantle discontinuity topography beneath Europe: Signature of akimotoite in subducting slabs. *Journal of Geophysical Research: Solid Earth*, *121*, 279–292. https://doi.org/10.1002/2015JB012452
Davies, G. F. (2006). Gravitational depletion of the early Earth's upper mantle and the viability of early plate tectonics. *Earth and Planetary Science Letters*, *243*(3), 376–382.
Deuss, A., Andrews, J., & Day, E. (2013). Seismic observations of mantle discontinuities and their mineralogical and dynamical interpretation. In *Physics and Chemistry of the Deep Earth* (chap. 10, pp. 297–323).
Deuss, A., Redfern, S. A., Chambers, K., & Woodhouse, J. H. (2006). The nature of the 660-kilometer discontinuity in Earth's mantle from global seismic observations of pP precursors. *Science*, *311*(5758), 198–201.
Diouane, Y. (2014). Globally convergent evolution strategies with application to Earth imaging problem in geophysics (Ph.D. thesis), Institut National Polytechnique de Toulouse.
Drilleau, M., Beucler, E., Mocquet, A., Verhoeven, O., Moebs, G., Burgos, G., et al. (2013). A Bayesian approach to infer radial models of temperature and anisotropy in the transition zone from surface wave dispersion curves. *Geophysical Journal International*, *195*(2), 1165–1183.
Duesterhoeft, E., & Capitani, C. (2013). THERIAK_D: An add-on to implement equilibrium computations in geodynamic models. *Geochemistry, Geophysics, Geosystems*, *14*, 4962–4967. https://doi.org/10.1002/ggge.20286
Duesterhoeft, E., Quinteros, J., Oberhaensli, R., Bousquet, R., & de Capitani, C. (2014). Relative impact of mantle densification and eclogitization of slabs on subduction dynamics: A numerical thermodynamic/thermokinematic investigation of metamorphic density evolution. *Tectonophysics*, *637*, 20–29.
Dziewonski, A. M., & Anderson, D. L. (1981). Preliminary reference Earth model. *Physics of the Earth and Planetary Interiors*, *25*(4), 297–356.
Efron, B., & Tibshirani, R. (1991). Statistical data analysis in the computer age. *Science*, *253*, 390–395.
Elshall, A. S., Pham, H. V., Tsai, F. T.-C., Yan, L., & Ye, M. (2015). Parallel inverse modeling and uncertainty quantification for computationally demanding groundwater-flow models using covariance matrix adaptation. *Journal of Hydrologic Engineering*, *20*(8), 4014,087.
Farra, V., & Vinnik, L. (2000). Upper mantle stratification by P and S receiver functions. *Geophysical Journal International*, *141*(3), 699–712.
Francis, D. (1987). Mantle-melt interaction recorded in spinel lherzolite xenoliths from the Alligator Lake volcanic complex, Yukon, Canada. *Journal of Petrology*, *28*(3), 569–597.
Frey, F., Green, D., & Roy, S. (1978). Integrated models of basalt petrogenesis: A study of quartz tholeiites to olivine melilitites from south eastern Australia utilizing geochemical and experimental petrological data. *Journal of Petrology*, *19*(3), 463–513.
Frost, D. J., & Dolejš, D. (2007). Experimental determination of the effect of H_2O on the 410–km seismic discontinuity. *Earth and Planetary Science Letters*, *256*(1-2), 182–195.
Fuchs, K., & Müller, G. (1971). Computation of synthetic seismograms with the reflectivity method and comparison with observations. *Geophysical Journal International*, *23*(4), 417–433.
Ghosh, S., Ohtani, E., Litasov, K. D., Suzuki, A., Dobson, D., & Funakoshi, K. (2013). Effect of water in depleted mantle on post-spinel transition and implication for 660 km seismic discontinuity. *Earth and Planetary Science Letters*, *371*, 103–111.
Grayver, A. V., & Kuvshinov, A. V. (2016). Exploring equivalence domain in nonlinear inverse problems using Covariance Matrix Adaption Evolution Strategy (CMAES) and random sampling. *Geophysical Journal International*, *205*(2), 971–987.
Grayver, A. V., Schnepf, N. R., Kuvshinov, A. V., Sabaka, T. J., Manoj, C., & Olsen, N. (2016). Satellite tidal magnetic signals constrain oceanic lithosphere-asthenosphere boundary. *Science Advances*, *2*(9), e1600798.
Hansen, N., & Ostermeier, A. (2001). Completely derandomized self-adaptation in evolution strategies. *Evolutionary Computation*, *9*(2), 159–195.
Hansen, N., Ros, R., Mauny, N., Schoenauer, M., & Auger, A. (2011). Impacts of invariance in search: When CMA-ES and PSO face ill-conditioned and non-separable problems. *Applied Soft Computing*, *11*(8), 5755–5769.
Hastings, W. K. (1970). Monte Carlo sampling methods using Markov chains and their applications. *Biometrika*, *57*(1), 97–109.
Hedlin, M. A., Shearer, P. M., & Earle, P. S. (1997). Seismic evidence for small-scale heterogeneity throughout the Earth's mantle. *Nature*, *387*(6629), 145–150.
Heit, B., Sodoudi, F., Yuan, X., Bianchi, M., & Kind, R. (2007). An S receiver function analysis of the lithospheric structure in South America. *Geophysical Research Letters*, *34*, L14307. https://doi.org/10.1029/2007GL030317
Helffrich, G. (2000). Topography of the transition zone seismic discontinuities. *Reviews of Geophysics*, *38*(1), 141–158.
Helffrich, G. (2006). Heterogeneity in the mantle—Its creation, evolution and destruction. *Tectonophysics*, *416*(1), 23–31.
Henderson, P., & Henderson, G. M. (2009). *The Cambridge handbook of Earth Science data*. Cambridge: Cambridge University Press.
Hirschmann, M. M. (2010). Partial melt in the oceanic low velocity zone. *Physics of the Earth and Planetary Interiors*, *179*(1-2), 60–71.
Hofmann, A., & Hart, S. (1978). An assessment of local and regional isotopic equilibrium in the mantle. *Earth and Planetary Science Letters*, *38*(1), 44–62.
Hofmann, A. W., & White, W. M. (1982). Mantle plumes from ancient oceanic crust. *Earth and Planetary Science Letters*, *57*(2), 421–436.
Irifune, T. (1993). Phase transformations in the Earth's mantle and subducting slabs: Implications for their compositions, seismic velocity and density structures and dynamics. *Island Arc*, *2*(2), 55–71.
Irifune, T. (1994). Absence of an aluminous phase in the upper part of the Earth's lower mantle. *Nature*, *370*(6485), 131–133.
Ita, J., & Stixrude, L. (1992). Petrology, elasticity, and composition of the mantle transition zone. *Journal of Geophysical Research*, *97*(B5), 6849–6866.
Jackson, I., & Faul, U. H. (2010). Grainsize-sensitive viscoelastic relaxation in olivine: Towards a robust laboratory-based model for seismological application. *Physics of the Earth and Planetary Interiors*, *183*(1-2), 151–163.
Jacobsen, B. H., & Svenningsen, L. (2008). Enhanced uniqueness and linearity of receiver function inversion. *Bulletin of the Seismological Society of America*, *98*(4), 1756–1767.
Kanamori, H., & Anderson, D. L. (1977). Importance of physical dispersion in surface wave and free oscillation problems. *Reviews of Geophysics*, *15*(1), 105–112.

Karato, S. (2010). Water distribution across the mantle transition zone and its implications for global material circulation. *Earth and Planetary Science Letters*, *301*(3), 413–423.
Katsura, T., Yoneda, A., Yamazaki, D., Yoshino, T., & Ito, E. (2010). Adiabatic temperature profile in the mantle. *Physics of the Earth and Planetary Interiors*, *183*(1-2), 212–218.
Kennett, B., & Engdahl, E. (1991). Traveltimes for global earthquake location and phase identification. *Geophysical Journal International*, *105*(2), 429–465.
Khan, A., Boschi, L., & Connolly, J. (2009). On mantle chemical and thermal heterogeneities and anisotropy as mapped by inversion of global surface wave data. *Journal of Geophysical Research*, *114*, B09305. https://doi.org/10.1029/2009JB006399
Khan, A., Connolly, J., & Olsen, N. (2006). Constraining the composition and thermal state of the mantle beneath Europe from inversion of long-period electromagnetic sounding data. *Journal of Geophysical Research*, *111*, B10102. https://doi.org/10.1029/2006JB004270
Khan, A., Liebske, C., Rozel, A., Rivoldini, A., Nimmo, F., Connolly, J., et al. (2018). A Geophysical Perspective on the Bulk Composition of Mars. *Journal of Geophysical Research: Planets*, *123*, 575–611. https://doi.org/10.1002/2017JE005371
Khan, A., Zunino, A., & Deschamps, F. (2013). Upper mantle compositional variations and discontinuity topography imaged beneath Australia from Bayesian inversion of surface-wave phase velocities and thermochemical modeling. *Journal of Geophysical Research: Solid Earth*, *118*, 5285–5306. https://doi.org/10.1002/jgrb50304
Kind, R., & Vinnik, L. (1988). The upper mantle discontinuities underneath the gRF array from P-to-S converted phases. *Journal of Geophysics*, *62*, 138–147.
Kind, R., Yuan, X. & Kumar, P. (2012). Seismic receiver functions and the lithosphere—asthenosphere boundary. *Tectonophysics*, *536*, 25–43.
Krischer, L., Hutko, A. R., Van Driel, M., Stähler, S., Bahavar, M., Trabant, C., & Nissen-Meyer, T. (2017). On-demand custom broadband synthetic seismograms. *Seismological Research Letters*, *88*(4), 1127–1140.
Kumar, P., Kind, R., Yuan, X., & Mechie, J. (2012). USarray receiver function images of the lithosphere-asthenosphere boundary. *Seismological Research Letters*, *83*(3), 486–491.
Langston, C. A. (1979). Structure under Mount Rainier, Washington, inferred from teleseismic body waves. *Journal of Geophysical Research*, *84*(B9), 4749–4762.
Langston, C. A., & Hammer, J. K. (2001). The vertical component P-wave receiver function. *Bulletin of the Seismological Society of America*, *91*(6), 1805–1819.
Lawrence, J. F., & Shearer, P. M. (2006a). A global study of transition zone thickness using receiver functions. *Journal of Geophysical Research*, *111*, B06307. https://doi.org/10.1029/2005JB003973
Lawrence, J. F., & Shearer, P. M. (2006b). Constraining seismic velocity and density for the mantle transition zone with reflected and transmitted waveforms. *Geochemistry, Geophysics, Geosystems*, *7*, Q10012. https://doi.org/10.1029/2006GC001339
Ligorria, J. P., & Ammon, C. J. (1999). Iterative deconvolution and receiver-function estimation. *Bulletin of the seismological Society of America*, *89*(5), 1395–1400.
Litasov, K. (2011). Physicochemical conditions for melting in the Earth's mantle containing a C–O–H fluid (from experimental data). *Russian Geology and Geophysics*, *52*(5), 475–492.
Liu, K. H. (2003). Effects of inelasticity on the apparent depth and detectability of seismic discontinuities in the mantle. *Geophysical research letters*, *30*(9), 1455. https://doi.org/10.1029/2002GL015264
Lodge, A., & Helffrich, G. (2009). Grid search inversion of teleseismic receiver functions. *Geophysical Journal International*, *178*(1), 513–523.
Lombardi, D., Braunmiller, J., Kissling, E., & Giardini, D. (2009). Alpine mantle transition zone imaged by receiver functions. *Earth and Planetary Science Letters*, *278*(3-4), 163–174.
Maguire, R., Ritsema, J., & Goes, S. (2018). Evidence of subduction-related thermal and compositional heterogeneity below the United States from transition zone receiver functions. *Geophysical Research Letters*, *45*, 8913–8922. https://doi.org/10.1029/2018GL078378
Mao, Z., Jacobsen, S. D., Jiang, F., Smyth, J. R., Holl, C. M., & Duffy, T. S. (2008). Elasticity of hydrous wadsleyite to 12 gPa: implications for Earth's transition zone. *Geophysical Research Letters*, *35*, L21305. https://doi.org/10.1029/2008GL035618
Mattern, E., Matas, J., Ricard, Y., & Bass, J. (2005). Lower mantle composition and temperature from mineral physics and thermodynamic modelling. *Geophysical Journal International*, *160*(3), 973–990.
McKenzie, D., & Bickle, M. (1988). The volume and composition of melt generated by extension of the lithosphere. *Journal of Petrology*, *29*(3), 625–679.
Metropolis, N., Rosenbluth, A. W., Rosenbluth, M. N., Teller, A. H., & Teller, E. (1953). Equation of state calculations by fast computing machines. *The Journal of Chemical Physics*, *21*(6), 1087–1092.
Monteiller, V., Chevrot, S., Komatitsch, D., & Fuji, N. (2012). A hybrid method to compute short-period synthetic seismograms of teleseismic body waves in a 3-D regional model. *Geophysical Journal International*, *192*(1), 230–247.
Moorkamp, M., Jones, A., & Fishwick, S. (2010). Joint inversion of receiver functions, surface wave dispersion, and magnetotelluric data. *Journal of Geophysical Research*, *115*, B04318. https://doi.org/10.1029/2009JB006369
Mosegaard, K., & Tarantola, A. (1995). Monte Carlo sampling of solutions to inverse problems. *Journal of Geophysical Research*, *100*(B7), 12,431–12,447.
Muller, G. (1985). The reflectivity method - a tutorial. *Journal of Geophysics-Zeitschrift Fur Geophysik*, *58*(1-3), 153–174.
Munch, F., Grayver, A., Kuvshinov, A., & Khan, A. (2018). Stochastic inversion of geomagnetic observatory data including rigorous treatment of the ocean induction effect with implications for transition zone water content and thermal structure. *Journal of Geophysical Research: Solid Earth*, *123*, 31–51. https://doi.org/10.1002/2017JB014691
Nakagawa, T., & Buffett, B. A. (2005). Mass transport mechanism between the upper and lower mantle in numerical simulations of thermochemical mantle convection with multicomponent phase changes. *Earth and Planetary Science Letters*, *230*(1), 11–27.
Nakagawa, T., Tackley, P. J., Deschamps, F., & Connolly, J. A. (2010). The influence of mORB and harzburgite composition on thermo-chemical mantle convection in a 3-D spherical shell with self-consistently calculated mineral physics. *Earth and Planetary Science Letters*, *296*(3-4), 403–412.
Nissen-Meyer, T., van Driel, M., Stähler, S. C., Hosseini, K., Hempel, S., Auer, L., et al. (2014). AxiSEM: broadband 3-D seismic wavefields in axisymmetric media. *Solid Earth*, *5*(1), 425–445.
Niu, F., & Kawakatsu, H. (1996). Complex structure of mantle discontinuities at the tip of the subducting slab beneath northeast China. *Journal of Physics of the Earth*, *44*(6), 701–711.
Oreshin, S., Kiselev, S., Vinnik, L., Prakasam, K. S., Rai, S. S., Makeyeva, L., & Savvin, Y. (2008). Crust and mantle beneath western Himalaya, Ladakh and western Tibet from integrated seismic data. *Earth and Planetary Science Letters*, *271*(1-4), 75–87.
Owens, T. J., Nyblade, A. A., Gurrola, H., & Langston, C. A. (2000). Mantle transition zone structure beneath Tanzania, East Africa. *Geophysical Research Letters*, *27*(6), 827–830.

Phinney, R. A. (1964). Structure of the Earth's crust from spectral behavior of long-period body waves. *Journal of Geophysical Research*, *69*(14), 2997–3017.

Ringwood, A. (1975). *Composition and Petrology of the Earth's Mantle*. New York: McGraw-Hill.

Ritsema, J., Cupillard, P., Tauzin, B., Xu, W., Stixrude, L., & Lithgow-Bertelloni, C. (2009). Joint mineral physics and seismic wave traveltime analysis of upper mantle temperature. *Geology*, *37*(4), 363–366.

Ritsema, J., Xu, W., Stixrude, L., & Lithgow-Bertelloni, C. (2009). Estimates of the transition zone temperature in a mechanically mixed upper mantle. *Earth and Planetary Science Letters*, *277*(1), 244–252.

Rondenay, S. (2009). Upper mantle imaging with array recordings of converted and scattered teleseismic waves. *Surveys in Geophysics*, *30*(4-5), 377–405.

Roy, C., & Romanowicz, B. (2017). On the implications of a-priori constraints in transdimensional Bayesian inversion for continental lithospheric layering. *Journal of Geophysical Research: Solid Earth*, *122*, 10,118–10,131. https://doi.org/10.1002/2017JB014968

Rychert, C. A., & Shearer, P. M. (2009). A global view of the lithosphere-asthenosphere boundary. *Science*, *324*(5926), 495–498.

Schmandt, B. (2012). Mantle transition zone shear velocity gradients beneath USArray. *Earth and Planetary Science Letters*, *355*, 119–130.

Schmandt, B., Jacobsen, S. D., Becker, T. W., Liu, Z., & Dueker, K. G. (2014). Dehydration melting at the top of the lower mantle. *Science*, *344*(6189), 1265–1268.

Schulze, K., Marquardt, H., Kawazoe, T., Ballaran, T. B., McCammon, C., Koch-Müller, M., et al. (2018). Seismically invisible water in Earth's transition zone? *Earth and Planetary Science Letters*, *498*, 9–16.

Shan, B., Afonso, J., Yang, Y., Grose, C., Zheng, Y., Xiong, X., & Zhou, L. (2014). The thermochemical structure of the lithosphere and upper mantle beneath south China: Results from multiobservable probabilistic inversion. *Journal of Geophysical Research: Solid Earth*, *119*, 8417–8441. https://doi.org/10.1002/2014JB011412

Shearer, P. M. (2000). Upper mantle seismic discontinuities. In S. Karato, et al. (Eds.), *Earth's deep Interior: Mineral Physics and Tomography from the Atomic to the Global Scale*, Geophysical Monograph Series (pp. 115–131). Washington, DC: American Geophysical Union.

Shen, J., Lorenzo, J. M., White, C. D., & Tsai, F. (2015). Soil density, elasticity, and the soil-water characteristic curve inverted from field-based seismic P-and S-wave velocity in shallow nearly saturated layered soils. *Geophysics*, *80*(3), WB11–WB19.

Shen, W., Ritzwoller, M. H., & Schulte-Pelkum, V. (2013). A 3-D model of the crust and uppermost mantle beneath the Central and Western US by joint inversion of receiver functions and surface wave dispersion. *Journal of Geophysical Research: Solid Earth*, *118*, 262–276. https://doi.org/10.1029/2012JB009602

Simmons, N., & Gurrola, H. (2000). Multiple seismic discontinuities near the base of the transition zone in the Earth's mantle. *Nature*, *405*(6786), 559–562.

Sobolev, A. V., Hofmann, A. W., Kuzmin, D. V., Yaxley, G. M., Arndt, N. T., Chung, S.-L., et al. (2007). The amount of recycled crust in sources of mantle-derived melts. *Science*, *316*(5823), 412–417.

Sodoudi, F., Yuan, X., Liu, Q., Kind, R., & Chen, J. (2006). Lithospheric thickness beneath the Dabie Shan, central eastern China from S receiver functions. *Geophysical Journal International*, *166*(3), 1363–1367.

Stixrude, L., & Lithgow-Bertelloni, C. (2005a). Mineralogy and elasticity of the oceanic upper mantle: Origin of the low-velocity zone. *Journal of Geophysical Research*, *110*, B03204. https://doi.org/10.1029/2004JB002965

Stixrude, L., & Lithgow-Bertelloni, C. (2005b). Thermodynamics of mantle minerals-I. Physical properties. *Geophysical Journal International*, *162*(2), 610–632.

Stixrude, L., & Lithgow-Bertelloni, C. (2011). Thermodynamics of mantle minerals-II. Phase equilibria. *Geophysical Journal International*, *184*(3), 1180–1213.

Tackley, P. J., Xie, S., Nakagawa, T., & Hernlund, J. W. (2005). Numerical and laboratory studies of mantle convection: Philosophy, accomplishments, and thermochemical structure and evolution. In R. D. van der Hilst, et al. (Eds.), *Earth's deep mantle: Structure, composition, and evolution*, Geophysical Monograph Series (Vol. 160, pp. 83–99). Washington, DC: American Geophysical Union.

Tarantola, A. (2005). *Inverse problem theory and methods for model parameter estimation*. Philadelphia: SIAM.

Tarantola, A., & Valette, B. (1982). Generalized nonlinear inverse problems solved using the least squares criterion. *Reviews of Geophysics*, *20*(2), 219–232.

Tauzin, B., Debayle, E., & Wittlinger, G. (2008). The mantle transition zone as seen by global PDS phases: No clear evidence for a thin transition zone beneath hotspots. *Journal of Geophysical Research*, *113*, B08309. https://doi.org/10.1029/2007JB005364

Tauzin, B., Kim, S., & Afonso, J.-C. (2018). Multiple phase changes in the mantle transition zone beneath Northeast Asia: Constraints from teleseismic reflected and converted body-waves. *Journal of Geophysical Research: Solid Earth*, *123*, 6636–6657. https://doi.org/10.1029/2017JB015238

Tauzin, B., Kim, S., & Kennett, B. (2017). Pervasive seismic low-velocity zones within stagnant plates in the mantle transition zone: Thermal or compositional origin? *Earth and Planetary Science Letters*, *477*, 1–13.

Tauzin, B., & Ricard, Y. (2014). Seismically deduced thermodynamics phase diagrams for the mantle transition zone. *Earth and Planetary Science Letters*, *401*, 337–346.

Tauzin, B., Van Der Hilst, R. D., Wittlinger, G., & Ricard, Y. (2013). Multiple transition zone seismic discontinuities and low velocity layers below western United States. *Journal of Geophysical Research: Solid Earth*, *118*, 2307–2322. https://doi.org/10.1002/jgrb.50182

Thio, V., Cobden, L., & Trampert, J. (2015). Seismic signature of a hydrous mantle transition zone. *Physics of the Earth and Planetary Interiors*, *250*, 46–63.

Tirone, M., Ganguly, J., & Morgan, J. (2009). Modeling petrological geodynamics in the Earth's mantle. *Geochemistry, Geophysics, Geosystems*, *10*, Q04012. https://doi.org/10.1029/2008GC002168

Van Driel, M., Krischer, L., Stähler, S. C., Hosseini, K., & Nissen-Meyer, T. (2015). Instaseis: Instant global seismograms based on a broadband waveform database. *Solid Earth*, *6*(2), 701–717.

Vinnik, L., Oreshin, S., Kosarev, G., Kiselev, S., & Makeyeva, L. (2009). Mantle anomalies beneath southern Africa: Evidence from seismic S and P receiver functions. *Geophysical Journal International*, *179*(1), 279–298.

Watt, J. P., Davies, G. F., & O'Connell, R. J. (1976). The elastic properties of composite materials. *Reviews of Geophysics*, *14*(4), 541–563.

Weidner, D. J. (1985). A mineral physics test of a pyrolite mantle. *Geophysical Research Letters*, *12*(7), 417–420.

Wood, B. J., & Holloway, J. R. (1984). A thermodynamic model for subsolidus equilibria in the system CaO – MgO – Al2O3 – SiO2. *Geochimica et Cosmochimica Acta*, *48*(1), 159 – 176.

Xie, S., & Tackley, P. J. (2004). Evolution of U-Pb and Sm-Nd systems in numerical models of mantle convection and plate tectonics. *Journal of Geophysical Research*, *109*, B11204. https://doi.org/10.1029/2004JB003176

Xu, W., Lithgow-Bertelloni, C., Stixrude, L., & Ritsema, J. (2008). The effect of bulk composition and temperature on mantle seismic structure. *Earth and Planetary Science Letters*, *275*(1), 70 – 79.

Yuan, X., Kind, R., Li, X. & Wang, R. (2006). The S receiver functions: synthetics and data example. *Geophysical Journal International*, *165*, 555 – 564. https://doi.org/10.1111/j.1365-246X.2006.02885.x

Zunino, A., Connolly, J., & Khan, A. (2011). Precalculated phase equilibrium models for geophysical properties of the crust and mantle as a function of composition. *Geochemistry, Geophysics, Geosystems*, *12*, Q04001. https://doi.org/10.1029/2010GC003304

Zunino, A., Khan, A., Cupillard, P., & Mosegaard, K. (2016). Constitution and structure of Earth's mantle: Insights from mineral physics and seismology. In A. Zunino, et al. (Eds.), *Integrated imaging of the Earth: Theory and applications*, Geophysical Monograph Series (Vol. 218, pp. 219 – 243). Washington, DC: American Geophysical Union.